Noncanonical Wnt/Ror2 signaling regulates cell–matrix adhesion to prompt directional tumor cell invasion in breast cancer

Hongjiang Si[a], Na Zhao[a], Andrea Pedroza[a], Ana-Maria Zaske[b], Jeffrey M. Rosen[a,c], Chad J. Creighton[c,d], and Kevin Roarty[a,c,*]

[a]Department of Molecular and Cellular Biology, [c]Breast Cancer Program, Dan L. Duncan Comprehensive Cancer Center, and [d]Department of Medicine, Baylor College of Medicine, Houston, TX 77030; [b]University of Texas Health Science Center at Houston, Houston, TX 77054

ABSTRACT **Cell–extracellular matrix (ECM) interactions represent fundamental exchanges during tumor progression, yet how particular signal-transduction factors prompt the conversion of tumor cells into migratory populations capable of systemic spread during metastasis remains elusive. We demonstrate that the noncanonical Wnt receptor, Ror2, regulates tumor cell–driven matrix remodeling and invasion in breast cancer. Ror2 loss-of-function (LOF) triggers the disruption of E-cadherin within tumor cells, accompanied by an increase in tumor cell invasion and collagen realignment in three-dimensional cultures. RNA sequencing of Ror2-deficient organoids further uncovered alterations in actin cytoskeleton, cell adhesion, and collagen cross-linking gene expression programs. Spatially, we pinpoint the up-regulation and redistribution of α_5 and β_3 integrins together with the production of fibronectin in areas of invasion downstream of Ror2 loss. Wnt/β-catenin–dependent and Wnt/Ror2 alternative Wnt signaling appear to regulate distinct functions for tumor cells regarding their ability to modify cell–ECM exchanges during invasion. Furthermore, blocking either integrin or focal adhesion kinase (FAK), a downstream mediator of integrin-mediated signal transduction, abrogates the enhanced migration observed upon Ror2 loss. These results reveal a critical function for the alternative Wnt receptor, Ror2, as a determinant of tumor cell–driven ECM exchanges during cancer invasion and metastasis.**

Monitoring Editor
Valerie Marie Weaver
University of California, San Francisco

Received: Feb 24, 2022
Revised: Jul 25, 2022
Accepted: Aug 18, 2022

INTRODUCTION

Early steps of cancer metastasis require that tumor cells actively invade and disseminate from the primary tumor to spread to secondary organs (Chiang and Massague, 2008). Such a process requires that tumor cells engage signaling pathways that enable remodeling of the actin cytoskeleton while simultaneously tuning cell–cell and cell–matrix adhesions during the invasion and cellular transit within

This article was published online ahead of print in MBoC in Press (http://www.molbiolcell.org/cgi/doi/10.1091/mbc.E22-02-0055) on August 24, 2022.

Conflict of interest: The authors declare no competing financial interests.

Author contributions: H. S., N. Z., A. P., A.-M. Z., and K. R. carried out the experiments and data analysis. C.J.C. analyzed the RNA sequencing data. K. R. and J.M.R. contributed to the design and implementation of the research. K. R. conceived the original idea and supervised the study. K. R. and H. S. wrote the manuscript with input from all authors. All authors discussed the results and provided critical feedback to shape the research, analysis, and manuscript preparation.

*Address correspondence to: Kevin Roarty (roarty@bcm.edu).

Abbreviations used: AFM, atomic force microscopy; Brdu, 5-Bromo-2′-deoxyuridine; BSA, bovine serum albumin; CAMII, Center for Advanced Microscopy and Image Informatics; CHP, collagen hybridizing peptide; CPRIT, Cancer Prevention and Research Institute of Texas; 3D, three-dimensional; DAPI, 4′,6-diamidino-2-phenylindole; DAVID, database for annotation, visualization and integrated discovery; DIC, differential interference contrast; Dkk1, Dikkopf-1; DLDCCC, Dan L. Duncan comprehensive cancer center; ECM, extracellular matrix; EMT, epithelial mesenchymal transition; ERM, ezrin, radixin, and moesin; FAK, focal adhesion kinase; FBS, fetal bovine serum; FN, fibronectin; Fpkm, fragment per kilobase of transcript per million mapped reads; GEM, genetically engineered mouse; GEMM, genetically engineered mouse model; GEO, gene expression omnibus; HBSS, Hanks' balanced salt solution; HRP, horseradish peroxidase; LOF, loss-of-function; LOX, lysyl oxidase; MLCII, myosin II light chain; MLCK, myosin light chain kinase; MOI, multiplicity of infection; NC, National Cancer Institute; NIH, National Institutes of Health; OiVM, Optical Imaging & Vital Microscopy; PBS, phosphate-buffered saline; PFA, paraformaldehyde; PVDF, Polyvinylidene fluoride; ROCK1, Rho-associated protein kinase 1; RT-qPCR, quantitative real-time PCR; shRNA, short hairpin RNA; TCGA, The Cancer Genome Atlas; TNBC, triple negative breast cancer.

the surrounding stroma (Friedl, 2004). Cellular and microenvironmental heterogeneity in cancer, together with variations in migration strategies, have hindered recent efforts to thwart the initial invasion and dissemination stages responsible for spurring cancer metastasis (Friedl and Alexander, 2011).

Wnt signaling is a known regulator of cell fate, migration, and polarity during key morphogenic embryonic and postnatal development events. Often such patterning requires simultaneous cell fate specification concomitantly with spatial positioning of the cells to achieve coordinated morphogenesis and dynamic cell movements (van Amerongen and Nusse, 2009). While canonical Wnt/β-catenin–dependent signals stabilize intracellular β-catenin and dictate self-renewal and cell-fate choices, alternative Wnt/β-catenin–independent cues coordinate various processes associated with cell movement, such as planar cell polarity and convergent extension (Angers and Moon, 2009). Like patterned organisms and tissues, tumors comprise a hierarchy of cell types with a range of molecular and phenotypic heterogeneity (Marusyk *et al.*, 2020). Such cellular diversity is often accompanied by the presence of spatial and temporal signaling changes during tumor progression; however, it remains unclear how such evolutionarily conserved pathways regulate tumor cell behaviors during cancer progression.

Extracellular matrix (ECM) reorganization often accompanies tumor cell invasion to provide an appropriate scaffold for tumor cell anchorage and rewires intracellular molecular signals that instigate tumor cell behaviors during cancer progression. In breast cancer, fibrosis and ECM stiffening are associated with poor prognosis in patients (Kauppila *et al.*, 1998; Provenzano *et al.*, 2008; Rottenberg *et al.*, 2008; Levental *et al.*, 2009). Matrix proteins like fibronectin are assembled with type I collagen and enable lysyl oxidase (LOX)- or LOX-like–dependent collagen cross-linking and organization (Erler *et al.*, 2009). Tumor cells respond to altered ECM composition primarily through integrin receptors, the physical link between the actin cytoskeleton within the cell and the outside ECM. Such cell–ECM interactions prompt focal adhesion kinase (FAK) autophosphorylation within the cell to reorganize its actin cytoskeleton, promote the assembly/disassembly of focal adhesion complexes, and apply traction forces to ECM proteins to facilitate directional cellular migration (McLean *et al.*, 2005). Like morphogenic and patterning processes in development, cancer cells undergo dynamic fluctuations in cell polarity, cytoskeletal organization, and cell–cell cohesion during cellular movement, highlighting the importance of tumor cell coordination and reciprocal engagement with their surrounding microenvironment (Franz *et al.*, 2002; Friedl and Gilmour, 2009). However, the precise regulation of such cellular behaviors and the signals that trigger invasive cell behavior in the context of cancer progression remain unknown.

We previously discovered that Wnt/β-catenin and Wnt/Ror2 alternative signaling are inversely correlated across breast cancers in The Cancer Genome Atlas (TCGA) (The Cancer Genome Atlas Network. 2012), and their coexistence within a given tumor is additionally marked by their anticorrelated nature across subpopulations of tumor cells (Roarty *et al.*, 2017). Although Wnt pathways are evolutionarily conserved signals that are essential for the development of multicellular organisms, how distinct but interconnected Wnt pathways regulate cancer progression remains unclear. We utilized a syngeneic TP53-null transplantable tumor model, a unique library of tumors representing human breast cancer subtypes at the molecular level (Jerry *et al.*, 2000; Zhang *et al.*, 2008; Herschkowitz *et al.*, 2012). TP53-mutated (typically missense and LOF) breast tumors make up 90% of triple negative breast cancers (TNBC) (Langerod *et al.*, 2007; Manie *et al.*, 2009). Collagen deposition and stromal remodeling, poor prognostic factors in breast cancer progression (Cox and Erler, 2011; Pickup *et al.*, 2014; Kai *et al.*, 2019), were highly present in tumors upon genetic deletion of Ror2 in genetically engineered mouse (GEM) models of TNBC. We, therefore, sought to interrogate how perturbations in Wnt/Ror2 signaling regulate the extracellular microenvironment and cell–ECM interactions important for tumor cell invasion and dissemination. We found that Ror2 status within primary tumors underlies the invasion propensity of tumor cells. Using three-dimensional (3D) tumor organoid models, we discovered altered gene expression programs associated with cell–cell adhesion, cytoskeletal remodeling, collagen fibril organization, and ECM integrity upon Ror2 loss. Heightened integrin-mediated signaling occurred within organoids as a consequence of enhanced integrin-α_5 and integrin-β_3 expression following Ror2 impairment. Interestingly, the matrisomal protein fibronectin (FN) was concomitantly up-regulated and assembled by Ror2-deficient tumor cells at sites of invasion. Consequently, we observed FAK activation and actin cytoskeleton alterations in Ror2-deficient tumor cells, leading to promigratory tumor cell behaviors. Inhibition of either integrin or FAK activation abrogated the increased invasion driven by Ror2 loss. Such changes were distinct from processes that regulated Wnt/β-catenin activation and offer insights into how canonical and alternative Wnt pathways coordinate cell–cell and cell–ECM adhesion during breast cancer progression.

RESULTS

Ror2 presence dictates tumor cell–directed collagen remodeling and transit through the ECM

In previous studies, we identified distinctions in the topology of canonical Wnt/β-catenin–dependent signaling activity and noncanonical β-catenin–independent Ror2-mediated Wnt signaling across subtypes of breast cancer and within subpopulations within tumors derived from the TNBC TP53-null GEM transplant model, which phenotypically and molecularly represent human breast cancer (Perou *et al.*, 2000; Herschkowitz *et al.*, 2007, 2012; Roarty *et al.*, 2017). We assigned a role for Ror2 in the regulation of cell state plasticity and adhesion dynamics within tumors, marked by heightened canonical Wnt/β-catenin signaling, yet we wanted to understand how Ror2 specifically regulates tumor cell invasion and dissemination, key initiating steps in metastasis (Roarty *et al.*, 2017). Across experimental models of TP53-null, basal-like TNBC, we observed that tumors deficient in Ror2 exhibited visible changes in the abundance and organization of the tumor stroma. We, therefore, sought to investigate how Wnt/Ror2 regulates the extracellular environment within TNBC tumors and subsequent tumor cell interactions with the ECM, central for tumor cell invasion and dissemination. Given that the ECM is an extensive part of the tumor microenvironment and collagens are the major structural proteins within the ECM, we first performed trichrome staining on control versus Ror2-deficient tumors, harboring lentiviral nontargeting shLUC or shRor2 constructs, respectively, to determine collagen composition upon Ror2 impairment. Interestingly, trichrome staining revealed a significant increase in collagen abundance and disorganized tumor stroma relative to Ror2-intact tumors (Figure 1, A and B). Notably, a twofold higher integrative density for collagen presence was uncovered within Ror2-depleted shRor2 tumors relative to shLUC control tumors (Figure 1C). Using a complementary collagen hybridizing peptide (CHP) that specifically binds to denatured collagen, we also detected a significant increase in collagen content within tumors following Ror2 depletion (Figure 1D). In control shLUC tumors, CHP presence was predominantly localized within the adjacent stroma surrounding tumor cells, while in shRor2 tumors, CHP was expanded in adjacent stromal areas, in addition to intercellular regions between

tumor cells (Figure 1D, arrows). Two-photon second harmonic microscopy further captured the heightened collagen fibril abundance and altered structure of collagen in vivo within Ror2-deficient tumors (Supplemental Figure S1A). These data implicate Wnt/Ror2 signaling as a regulator of collagen remodeling, prompting us to explore how Ror2 status specifically regulates tumor cell–matrix interactions during tumor progression.

We established 3D tumor organoid cultures within type I collagen ECM to evaluate the impact of Ror2 depletion on cell–ECM exchanges during cancer invasion (Roarty *et al.*, 2017). Collagen I is the most abundant scaffolding protein present in tissues, and its cross-linking is highly associated with breast cancer risk (Levental *et al.*, 2009). Given the altered collagen abundance in primary tumors observed upon Ror2 depletion, we reasoned that Wnt/Ror2 signaling could provide tumor cell intrinsic instruction by dictating ECM composition and remodeling, facilitating the adhesion to and invasion of tumor cells through the microenvironment. Accordingly, we generated tumor organoids using two independent GEM TP53-null transplant models (Jerry *et al.*, 2000; Roarty *et al.*, 2017) representative of the basal-like subtype of TNBC (2225L and 2153L) to probe the functional implications of Wnt/Ror2 biology on cell–matrix interactions during tumor progression. Notably, Ror2 knockdown by lentiviral short hairpin RNA (shRNA) prompted the active invasion of tumor cells into the surrounding collagen-rich matrix, accompanied by 4.5- and 3.7-fold increases in protrusive tumor cell extensions from 2225L- and 2153L-shRor2 organoids, respectively, as compared with noninvading control shLUC organoids (Figure 1, E and F; Supplemental Movies 1 and 2). The extent of invasion into the surrounding ECM, based on the distance of disseminating protrusions emanating from each organoid, was also expanded upon Ror2 loss within both the 2225L and 2153L TP53-null TNBC models (Figure 1G). Such invasion from Ror2-deficient tumors cells was also accompanied by the realignment of collagen fibrils within the surrounding ECM. Collagen fibril alignment was quantified by selecting regions of interest within ECM positioned perpendicular to the organoid–ECM border (Figure 1, H–J). In shRor2 organoid cultures, there was a threefold heightened change in directionality of the collagen fibrils compared with shLUC organoids (Figure 1J), demonstrating that Ror2-deficient tumor cells support local changes in collagen remodeling.

We next reasoned that epithelial-to-mesenchymal transition (EMT) could be involved in triggering cellular invasion downstream of Ror2 LOF, given our previous observations that Ror2 regulates the claudin-low/mesenchymal subpopulation presence in TNBC (Roarty *et al.*, 2017). Ror2 depletion decreased E-cadherin abundance (Figure 1N), yet mesenchymal markers like vimentin and core EMT-related genes (*Zeb1*, *Snai1*, and *Snai2)* remained unchanged (Figure 1, O and P). Notably, shRor2 organoids exhibited a discontinuous pattern of E-cadherin at the adherens junctions relative to control shLUC organoids, which maintain a continuous junctional E-cadherin profile by immunostaining (Figure 1, K–M). The extent of E-cadherin loss in shRor2 organoids was most pronounced at the invasive front of cells migrating from the organoid body into the surrounding ECM (Figure 1, K and L, * insets). Though vimentin expression levels remained unchanged upon Ror2 depletion, a shift in vimentin localization was observed in areas corresponding with heightened tumor cell invasion into the ECM (Figure 1, K and L, inset arrows, and O). Thus, the disruption in E-cadherin expression and lack of change in mesenchymal markers suggest that cell–cell adhesion is compromised upon Ror2 depletion rather than a complete shift from an epithelial to a mesenchymal state. Depleting Ror2 within GEM models of TNBC thus decreases E-cadherin expression in tumor cells, likely initiating cellular invasion in 3D organoids and the reorientation and remodeling of collagenous ECM in vitro and in vivo.

Ror2 loss prompts alterations in actin cytoskeleton and cell–ECM dynamics

The enhanced degree of invasion in tumor organoids in vitro and increased collagen content in vivo upon Ror2 depletion prompted us to explore whether Wnt/Ror2 signaling maintains appropriate intercellular and cell–matrix interactions, the disruption of which prompts an invasive phenotype for tumor cells. Accordingly, we performed RNA sequencing on 4-day cultures of 3D shLUC versus shRor2 tumor organoids within type I collagen, derived from two basal-like TP53-null GEM models of TNBC (Figure 2A; Supplemental Figure S1B). Gene ontology programs encompassing the guidance of tumor cell movement, particularly the regulation of cell migration, cell–cell adhesion, integrin-mediated adhesion, collagen fibril organization, and cytoskeletal organization, were highly represented in tumor cells upon *Ror2* knockdown (Figure 2, B–D; Supplemental Figure S1C). Given the manifestation of collagen fibril expansion upon Ror2 loss, we investigated how Ror2 presence regulates intercellular cohesion and engagement with the ECM microenvironment during cancer invasion. Interestingly, Lox and Lox-like 2 (Loxl2), enzymes required for the biogenesis and cross-linking of fibrillar collagen, were significantly up-regulated upon Ror2 depletion at the RNA and protein levels (Figure 2, C and D), along with tumor cell intrinsic collagen expression (Figures 1, B–D, and 2, B–D; Supplemental Figure S1A). Interestingly, α_5 integrin and β_3 integrin, cell-surface receptors for ECM components responsible for physically bridging internal and external filamentous networks to enable transmission of signals across the plasma membrane, were also increased in tumor cells following Ror2 depletion (Figure 2, D–F; Supplemental Figure S1D). These results demonstrate that Wnt/Ror2 signaling regulates both cadherin-based adherens junctions and integrin-based adhesion gene expression programs within TNBC tumor cells, the balance of which is likely critical for actin cytoskeletal rearrangements, cell–matrix cross-talk, and coordination of cellular invasion.

Loss of Ror2 triggers the up-regulation and redistribution of integrins to assemble fibronectin at sites of invasion

Integrins bind ECM proteins and are responsible for enabling cells to sense mechanical signals from the surrounding microenvironment and to transmit such signals to the actin cytoskeleton (Hynes, 1992). We thus explored Ror2's role in regulating integrin–ECM engagement upon impaired homotypic E-cadherin expression, given the observed collagen alterations in vivo and representation of integrin-based cell–substrate adhesion gene programs upon Ror2 disruption. In shRor2 organoids, we discovered that α_5 integrin was up-regulated at both RNA and protein levels relative to control shLUC organoids (Figure 2, C–F). We additionally detected an increase in β_3 integrin by flow cytometry upon Ror2 loss (Supplemental Figure S1D). Interestingly, analysis of tumor organoids by immunofluorescence revealed the up-regulation of α_5 integrin within Ror2-deficient organoids, particularly prevalent at sites of tumor cell invasion within the surrounding type I collagen matrix (Figure 2, G and H). These data suggest that loss of Wnt/Ror2 signaling in TNBC tumor cells can alter both cell–cell and cell–ECM signaling, likely important for coordinating tumor cell transit.

Along with their roles in cell adhesion, migration, and bidirectional signaling, integrins also mediate fibronectin matrix assembly, particularly through integrin $\alpha5\beta1$ (Wu *et al.*, 1993; Sechler *et al.*, 1996; Pankov *et al.*, 2000). Importantly, the deposition and restructuring of collagen in the ECM depends on the presence and stability

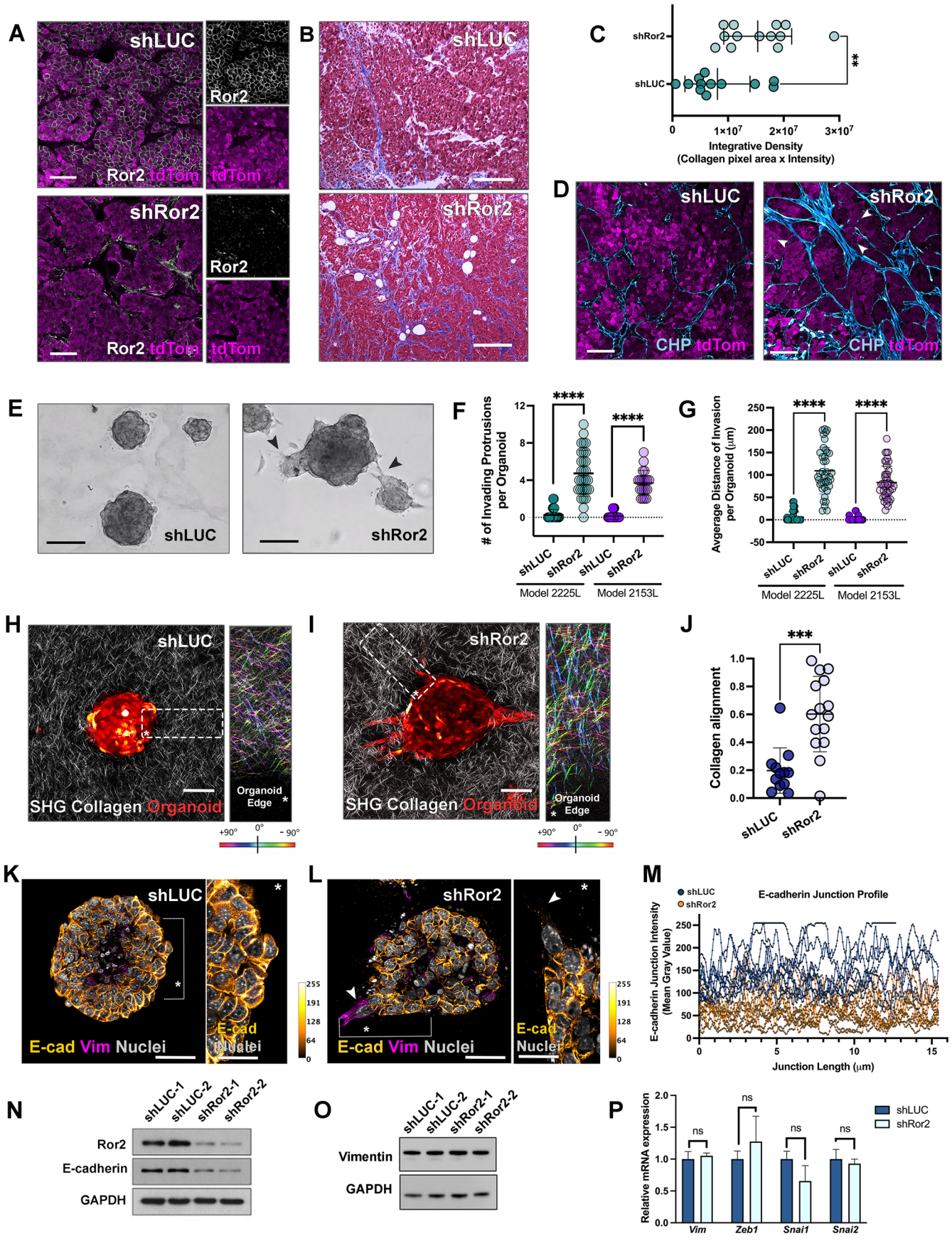
A
shLUC
Ror2
Ror2 tdTom
tdTom
shRor2
Ror2
Ror2 tdTom
tdTom
B
shLUC
shRor2
C
shRor2
shLUC
**
0
1×10^7
2×10^7
3×10^7
Integrative Density
(Collagen pixel area x Intensity)
D
shLUC
CHP tdTom
shRor2
CHP tdTom
E
shLUC
shRor2
F
# of Invading Protrusions per Organoid
****
****
shLUC
shRor2
shLUC
shRor2
Model 2225L
Model 2153L
G
Avgerage Distance of Invasion per Organoid (μm)
****
****
shLUC
shRor2
shLUC
shRor2
Model 2225L
Model 2153L
H
shLUC
SHG Collagen Organoid
Organoid Edge
+90°
0°
- 90°
I
shRor2
SHG Collagen Organoid
Organoid Edge
+90°
0°
- 90°
J
***
Collagen alignment
shLUC
shRor2
K
shLUC
E-cad Vim Nuclei
E-cad Nuclei
255
191
128
64
0
L
shRor2
E-cad Vim Nuclei
E-cad Nuclei
255
191
128
64
0
M
shLUC
shRor2
E-cadherin Junction Profile
E-cadherin Junction Intensity (Mean Gray Value)
Junction Length (μm)
N
shLUC-1
shLUC-2
shRor2-1
shRor2-2
Ror2
E-cadherin
GAPDH
O
shLUC-1
shLUC-2
shRor2-1
shRor2-2
Vimentin
GAPDH
P
Relative mRNA expression
ns
ns
ns
ns
shLUC
shRor2
Vim
Zeb1
Snai1
Snai2

of fibronectin. We discovered that fibronectin protein levels were elevated following Ror2 loss in tumor organoids (Figure 2L). This increase was at the posttranscriptional level, because we did not detect induction of fibronectin mRNA (Figure 2, A and L). Moreover, like α_5 integrin, fibronectin was up-regulated and spatially repositioned adjacent to the invading cells disseminating from the organoid body upon Ror2 loss, particularly at the sites of cell protrusions into the ECM (Figure 2, M and N). Intriguingly, the in vivo intratumoral topology of both α_5 integrin and fibronectin expanded from the tumor periphery in controls to a more sizeable area encompassing both the periphery and inner tumor mass following Ror2 loss (Figure 2, I–K, and O–Q). Though integrin and fibronectin presence were noted in the adjacent stromal regions within both shLUC and shRor2 tumors, tumor cell intrinsic expression was uniquely apparent in Ror2-deficient tumors based on an increase in mean fluorescence intensity within tumor cell–labeled tdTomato+ regions (Figure 2, I–K, and O–Q). Collectively, these data suggest that Wnt signaling through Ror2 regulates tumor cell–derived fibronectin expression along with its receptor, Itga5, likely important for balancing spatiotemporal states of cell adhesion and invasion during tumor progression.

Focal adhesions and actin cytoskeleton dynamics are regulated by Ror2

Integrin-linked focal adhesion complexes serve as a physical scaffold for the cell to adhere to the exterior ECM and additionally interact with the interior actin cytoskeleton, providing instructive and highly tunable cues necessary for modulating adhesion and passage through the ECM (McLean *et al*., 2005). FAK is activated downstream of integrins, typically in response to integrin clustering. Given the up-regulation and localization of α_5 integrin at plasma membrane sites of invasion in Ror2-deficient tumor organoids, we asked whether integrin presence is also accompanied by changes in the activation of FAK within Ror2-LOF organoids. By Western blot analysis, the level of pFAK was elevated in Ror2-deficient tumor organoids (Figure 3A), and this observation was confirmed by pFAK immunofluorescence in 3D tumor organoids (Figure 3, B and C, boxed insets). In vivo, we observed the prevalence of pFAK within tumor cells located within the tumor periphery, while pFAK levels were negligible within the tumor body central to the tumor margin in controls (Figure 3, D, Di-ii, E, and Ei-ii insets). Interestingly, Ror2-depleted tumors had an overall increase in pFAK activation throughout the tumor, in contrast to negligible levels of pFAK within the body of control tumors, demonstrating that the pFAK presence was expanded spatially in tumors following Ror2 loss (Figure 3, D and E, insets, and F). These results reveal the significant change in focal adhesion topology dictated by the presence of Wnt/Ror2 signaling in vivo (Figure 3, A–F).

We suspected that actin cytoskeletal dynamics were changed following integrin-mediated FAK activation upon Ror2 LOF, as indicated by RNA sequencing analysis (Figure 2A). Actin cytoskeletal remodeling is a cyclical process necessary for locomotion and shape demands of the cell, requiring actin-binding proteins (ABPs) and fluctuations in globular monomeric (G) and filamentous (F) actin. Indeed, actin-based cytoskeletal rearrangements were identified based on the evaluation of F-actin/G-actin turnover (Figure 3, G and H). Ror2-depleted tumor cells exhibited an almost fourfold higher

FIGURE 1: Wnt/Ror2 regulates tumor cell–directed collagen remodeling and invasion. (A) Immunofluorescence for Ror2 protein in TP53-null 2225L basal-like GEM models (Cyan—Ror2, tdTomato—LeGO-hairpin transduced tumor cells). (B) Representative trichrome staining of basal-like 2225L TP53-null mammary tumors showing collagen abundance (blue) and tumor organization in shLUC and shRor2 tumor sections. Scale 50 μm. (C) Quantification of trichrome collagen abundance by Integrative Density (collagen pixel area X fluorescence intensity, $n = 4$ tumors per group, four fields per tumor, $^{**}p < 0.01$). (D) Collagen hybridizing peptide histopathology (CHP-Alexa488, pseudocolored Cyan hot LUT) within shLUC and shRor2 2225L tumors (tdTomato—tumor cells, cyan). (E) Brightfield DIC images of shLUC and shRor2 2225L tumor organoids in type I collagen. Scale 50 μm. Ror2-depleted organoids exhibit increased number and extent of invasive projections. (F) Quantitation of the number of protrusions disseminated from Ror2-depleted organoids within the basal-like 2225L and 2153L TP53-null models. 2225L shLUC 0.2 ± 0.58 vs. shRor2 4.73 ± 2.47 and 2153L shLUC 0.15 ± 0.33 vs. shRor2 3.7 ± 1.3 invasive nodes. Representative quantitation of three independent experiments ($n = 30$ organoids per group, $^{****}p < 0.0001$, $^{***}p < 0.001$). (G) Quantitation of distance of invading tumor cell projections in micrometers measured from the edge of the organoid body. The average distance is represented for each organoid within shLUC and shRor2 groups. 2225L shLUC 5.9 ± 11.49 μm vs. shRor2 109.3 ± 52 μm and 2153L shLUC 2.0 ± 5.5 μm vs. shRor2 83.02 ± 36.63 μm. Representative quantitation of three independent experiments ($n = 40$–50 organoids per group, $^{****}p < 0.0001$, $^{***}p < 0.001$). (H, I) Second harmonic confocal imaging for collagen (white) and tdTomato (red) showing collagen fibril reorganization upon Ror2 loss. Regions of interest are denoted as dashed boxes to depict representative areas where collagen fiber directionality was measured perpendicular to the organoid body with the OrientationJ plug-in in ImageJ. Pseudocoloring of the insets indicates orientation angles from –90° to 90°; realignment with the organoids is defined as 1 and depicted in the range of blue, cyan, green. Scale 80 μm. (J) Quantitation of collagen alignment based on regions of interest in H and I across 15–20 organoids. Alignment was increased in shRor2 organoids relative to lack of alignment in shRor2 organoids, shLUC 0.19 ± 0.16 vs. shRor2 0.60 ± 0.27. (K, L) Immunofluorescence of E-cadherin (pseudocolored orange hot LUT), vimentin (magenta), and nuclei (gray) in 2225L (K) shLUC and (L) shRor2 organoids, showing down-regulated E-cadherin and altered distribution of vimentin upon Ror2 loss. K* inset shows E-cadherin continuity within shLUC organoids. L* inset shows discontinuity and loss of E-cadherin in shRor2 organoids. Scale 50 μm, *Insets 25 μm. Arrows denote areas of invasion with most down-regulated levels of E-cadherin and redistributed vimentin. (M) Quantitation of the junctional profile of E-cadherin at multiple individual cell junctions within shLUC and shRor2 organoids. E-cadherin levels are depicted as mean gray values from 0 to 255 pixel density over a 10–15 μm distance using the ImageJ segmented line tool. (N) Western blot of 2225L shLUC and shRor2 organoids for Ror2 and E-cadherin, revealing decreased Ror2 and E-cadherin expression levels in shRor2 organoids. (O) Western blot of 2225L shLUC and shRor2 organoids for vimentin. (P) Quantitative SYBR Green RT-qPCR measurement of mesenchymal markers (*Vim*, *Zeb1*, *Snai1*, and *Snai2*) in 2225L shLUC vs. shRor2 tumor cells from organoid cultures. Gene expression levels of the shRor2 group are represented relative to the control shLUC group, and fold changes were plotted (ns: not significant; *P* values = 0.51, 0.31, 0.09, and 0.50, respectively; $n = 3$ biological replicates for each group).

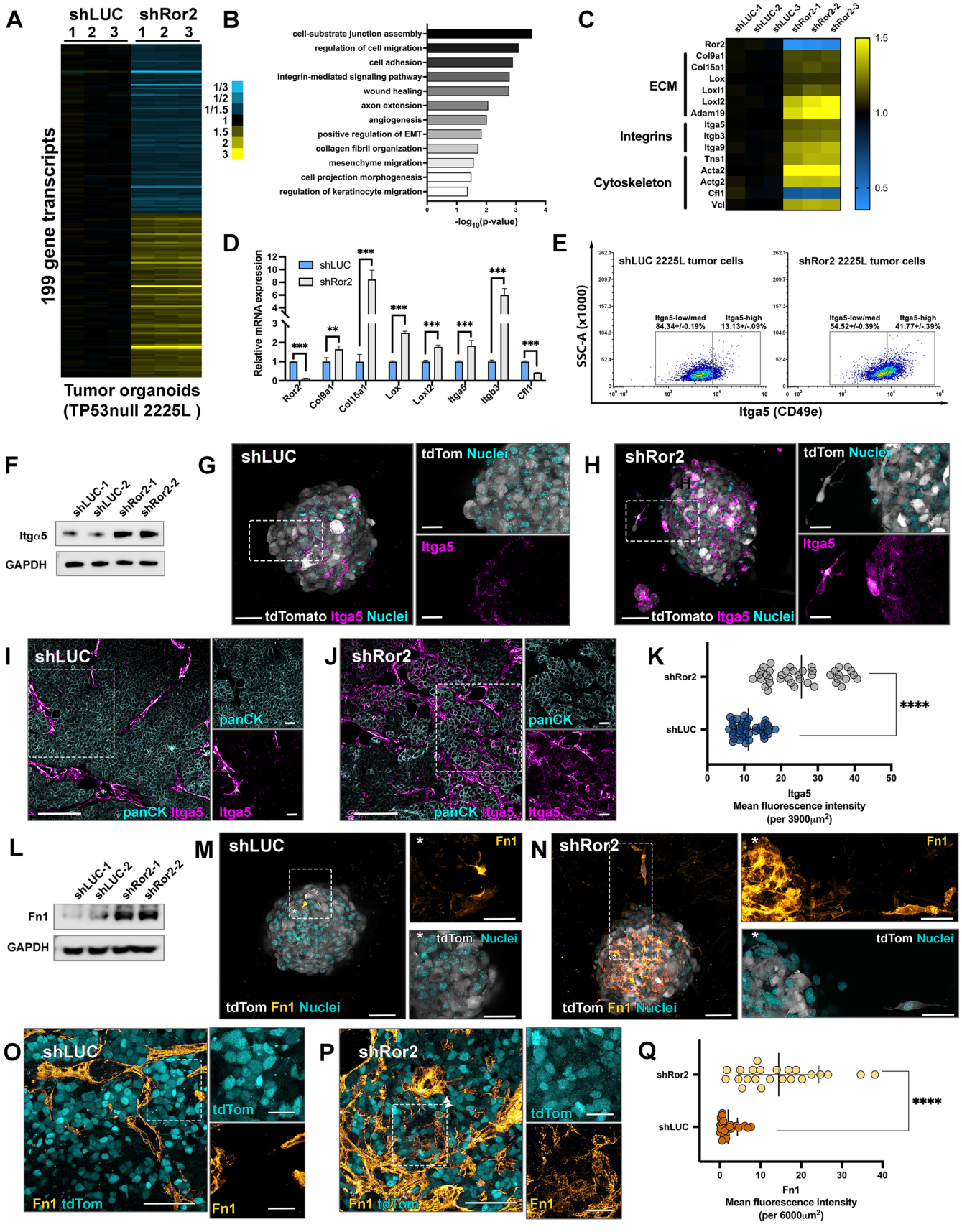
A
shLUC
shRor2
1 2 3 1 2 3
199 gene transcripts
1/3
1/2
1/1.5
1
1.5
2
3
Tumor organoids
(TP53null 2225L)
B
cell-substrate junction assembly
regulation of cell migration
cell adhesion
integrin-mediated signaling pathway
wound healing
axon extension
angiogenesis
positive regulation of EMT
collagen fibril organization
mesenchyme migration
cell projection morphogenesis
regulation of keratinocyte migration
-log10(p-value)
C
shLUC-1
shLUC-2
shLUC-3
shRor2-1
shRor2-2
shRor2-3
ECM
Integrins
Cytoskeleton
Ror2
Col9a1
Col15a1
Lox
Loxl1
Loxl2
Adam19
Itga5
Itgb3
Itga9
Tns1
Acta2
Actg2
Cfl1
Vcl
1.5
1.0
0.5
D
Relative mRNA expression
shLUC
shRor2
Ror2
Col9a1
Col15a1
Lox
Loxl2
Itga5
Itgb3
Cfl1
E
shLUC 2225L tumor cells
shRor2 2225L tumor cells
Itga5-low/med
84.34+/-0.19%
Itga5-high
13.13+/-.09%
Itga5-low/med
54.52+/-0.39%
Itga5-high
41.77+/-.39%
SSC-A (x1000)
Itga5 (CD49e)
F
shLUC-1
shLUC-2
shRor2-1
shRor2-2
Itgα5
GAPDH
G
shLUC
tdTom Nuclei
Itga5
tdTomato Itga5 Nuclei
H
shRor2
tdTom Nuclei
Itga5
tdTomato Itga5 Nuclei
I
shLUC
panCK
panCK Itga5
Itga5
J
shRor2
panCK
panCK Itga5
Itga5
K
shRor2
shLUC
****
Itga5
Mean fluorescence intensity
(per 3900μm2)
L
shLUC-1
shLUC-2
shRor2-1
shRor2-2
Fn1
GAPDH
M
shLUC
Fn1
tdTom Nuclei
tdTom Fn1 Nuclei
N
shRor2
Fn1
tdTom Nuclei
tdTom Fn1 Nuclei
O
shLUC
tdTom
Fn1 tdTom
Fn1
P
shRor2
tdTom
Fn1 tdTom
Fn1
Q
shRor2
shLUC
****
Fn1
Mean fluorescence intensity
(per 6000μm2)

level of filamentous (F) to monomeric (G) actin relative to Ror2-intact tumor cells (Figure 3, G and H). In 3D organoids, F-actin localization was evident within the cell cortex of tumor cells within control shLUC organoids; however, this ring-like organization between cells shifted in distribution upon Ror2 depletion, yielding formation of F-actin stress fibers within the organoid body and invading cellular protrusions (Figure 3, I and J, insets). We further evaluated F-actin and pFAK distribution in tumor cells cultured in 2D and observed the augmentation of F-actin–rich filipodia and F-actin stress fiber assembly in shRor2 cells compared with shLUC control tumor cells (Figure 3, K and L). Moreover, increased pFAK levels were prominent within F-actin–rich filopodia expanded upon Ror2 loss (Figure 3, K and L; Supplemental Movies 3 and 4). The change in F-actin and pFAK activation in shRor2 cells were further corroborated by assessing the mechanical differences between shLUC and shRor2 tumor cells. Atomic force microscopy (AFM) revealed that shRor2 tumor cells harbored a 1.6-fold higher Young's modulus relative to more elastic shLUC tumor cells with intact Ror2 expression (Figure 3, M and N). Such findings support that Wnt/Ror2 signals normally maintain actin cytoskeletal homeostasis within tumor cells by maintaining appropriate actin turnover and cell elasticity.

Given the changes in F-actin dynamics and cellular mechanics upon Wnt/Ror2 disruption, we assessed the intracellular signaling downstream of Ror2 LOF and identified a decrease in Rho-associated protein kinase 1 (ROCK1) and its effector, RhoA, in tumor organoids (Figure 3O), as previously observed (Roarty *et al.*, 2017). Both myosin light chain kinase (MLCK) and ROCK1 can phosphorylate myosin II light chain (MLCII), a key mediator of cellular contraction. Although levels of MLCK were intact upon Ror2 loss, MLC phosphorylation was decreased (Figure 3P), likely impacting the assembly of F-actin stress fibers and focal adhesions. Moreover, cofilin, a key actin-binding protein responsible for the depolymerization of filamentous F-actin (Kanellos and Frame, 2016), was significantly down-regulated in tumor organoids in vitro and within tumors in vivo upon Ror2 loss (Figure 3Q; Supplemental Figure S2, A and B). Cofilin down-regulation was not attributed to Wnt/β-catenin activation upon Ror2 loss, as we tested Wnt/β-catenin LOF in shLUC and shRor2 organoids by conditionally overexpressing a dominant negative form of TCF4 to prevent the β-catenin-TCF/LEF interaction and repress transcription of canonical Wnt target genes (Bocchi *et al.*, 2017). dnTCF4 inhibition of Wnt/β-catenin activation failed to rescue cofilin loss in the context of Ror2 knockdown (Figure 4I; Supplemental Figure S3A). In vivo, we detected an increase in the extent of p-Ser3 cofilin at the periphery of shRor2 tumors relative to a very narrow zone directly abutting the tumor-stromal interface in shLUC control tumors (Supplemental Figure S2B). Ser3 phosphorylation inactivates cofilin, suggesting that heightened p-cofilin levels following Ror2 loss likely contribute to actin filament elongation, an increase in the F/G actin ratio, and the invasive potential of tumor cells. Finally, ezrin, radixin, and moesin (ERM), linkers of the actin cytoskeleton to the plasma membrane, were phosphorylated/activated at the periphery of control shLUC tumors but were expanded spatially throughout the tumor body upon Ror2 loss (Supplemental Figure S2, C and C').

FIGURE 2: Ror2 depletion promotes gene expression alterations related to cell–ECM interactions, reshaping integrin signaling and ECM composition. (A) Heatmap display of significantly differentially expressed genes ($p < 0.01$, *t* test using log2-transformed values and fold change >1.2) in 2225L shLUC and shRor2 organoids by RNA sequencing. Fold changes are represented by two-way gradients to blue (down-regulation) and yellow (up-regulation). (B) Gene ontology analysis by DAVID Bioinformatics Database demonstrating the enrichment of gene expression in several biological processes upon Ror2 loss. (C) Heatmap display of highlighted genes in 2225L shLUC and shRor2 organoid RNA sequencing related to cell–ECM interaction, integrin signaling, and cytoskeleton reorganization. Fold changes are represented by two-way gradients to blue (down-regulation) and yellow (up-regulation). (D) RT-qPCR measurement of highlighted genes in 2225L shLUC and shRor2 cells for representative genes from C. Gene expression levels were normalized to GAPDH, and the shRor2 group is represented relative to the shLUC group. Fold changes are graphed (***$p < 0.0001$; **$p < 0.001$; $n = 3$ for each group). (E) Flow cytometry analysis for α_5 integrin Itga5 (CD49e) on shLUC and shRor2 tumor cells from the 2225L TP53-null GEM model. shRor2 tumors exhibit an increase in Itga5 expression with an approximately threefold increase in Itga5-high cells upon Ror2 loss (10,000 single-cell events analyzed per tumor; plots represent $n = 3$ tumors per group; representative of three independent experiments). (F) Western blot of 2225L shLUC and shRor2 organoids for Itga5, showing increased Itga5 expression levels in Ror2-depleted organoids. (G, H) 3D immunofluorescence of integrin $\alpha5$ (magenta LUT), tdTomato (gray), and nuclei (cyan) in (G) 2225L shLUC and (H) shRor2 organoids, showing up-regulated integrin $\alpha5$ upon Ror2 loss, particularly in invading projections and within disseminated cells (arrows). Scale 50 μm. Insets represent a 6 μm cross-section of each organoid, insets 20 μm scale. (I) Immunofluorescence of α_5 integrin (magenta), pan-keratin (cyan) in 2225L shLUC primary tumor sections, showing topographic distribution of α_5 integrin in control tumors. Inset represent boxed magnified regions. Scale 100 μm. Insets 20 μm. (J) Representative immunofluorescence of α_5 integrin (magenta), pan-keratin (cyan) in 2225L shRor2 primary tumor sections, showing enhanced α_5 integrin expression within tumor cells in shRor2 tumors. Scale 100 μm. Insets 20 μm. (K) Quantitation of Itga5 mean fluorescence intensity in H and I per 3900 mm^2 area ($n = 6$ tumors per shLUC and shRor2 group; ****$p < 0.00001$). (L) Western blot of 2225L shLUC and shRor2 organoids for Fn1, showing increased Fn1 expression levels in Ror2-depleted organoids. (M, N) 3D Immunofluorescence of Fn1 (orange hot LUT), tdTomato+ tumor cells (gray), and nuclei (cyan) in 2225L. Scale 50 μm, Insets 35 μm. (M) shLUC organoids and (N) 2225L shRor2 organoids, showing increased Fn1 deposition upon Ror2 loss, specifically around invasive projections at the tumor cell–matrix interface. Insets represent magnified areas of boxed regions. Scale 35 μm. (O, P) Immunofluorescence of Fn1 (orange hot LUT), tdTomato tumor cells (cyan) in (O) 2225L shLUC primary tumor sections, showing deposition of Fn1 predominantly within adjacent stromal regions surrounding tumor cells. Scale 50 μm. Inset scale 20 μm. (P) Immunofluorescence of Fn1 (orange hot LUT), tdTomato tumor cells (cyan) in 2225L shRor2 primary tumor sections, showing increased tumor cell–intrinsic Fn1 deposition in shRor2 tumors (arrows) along with adjacent stromal Fn1 presence. Insets are magnified areas of boxed regions. Inset scale 20 μm. (Q) Quantitation of mean fluorescence intensity per 6000 μm^2 area measured across shLUC and shRor2 tumors. Regions of interest quantified were tdTomato+ to denote tumor cell–derived Fn1 expression.

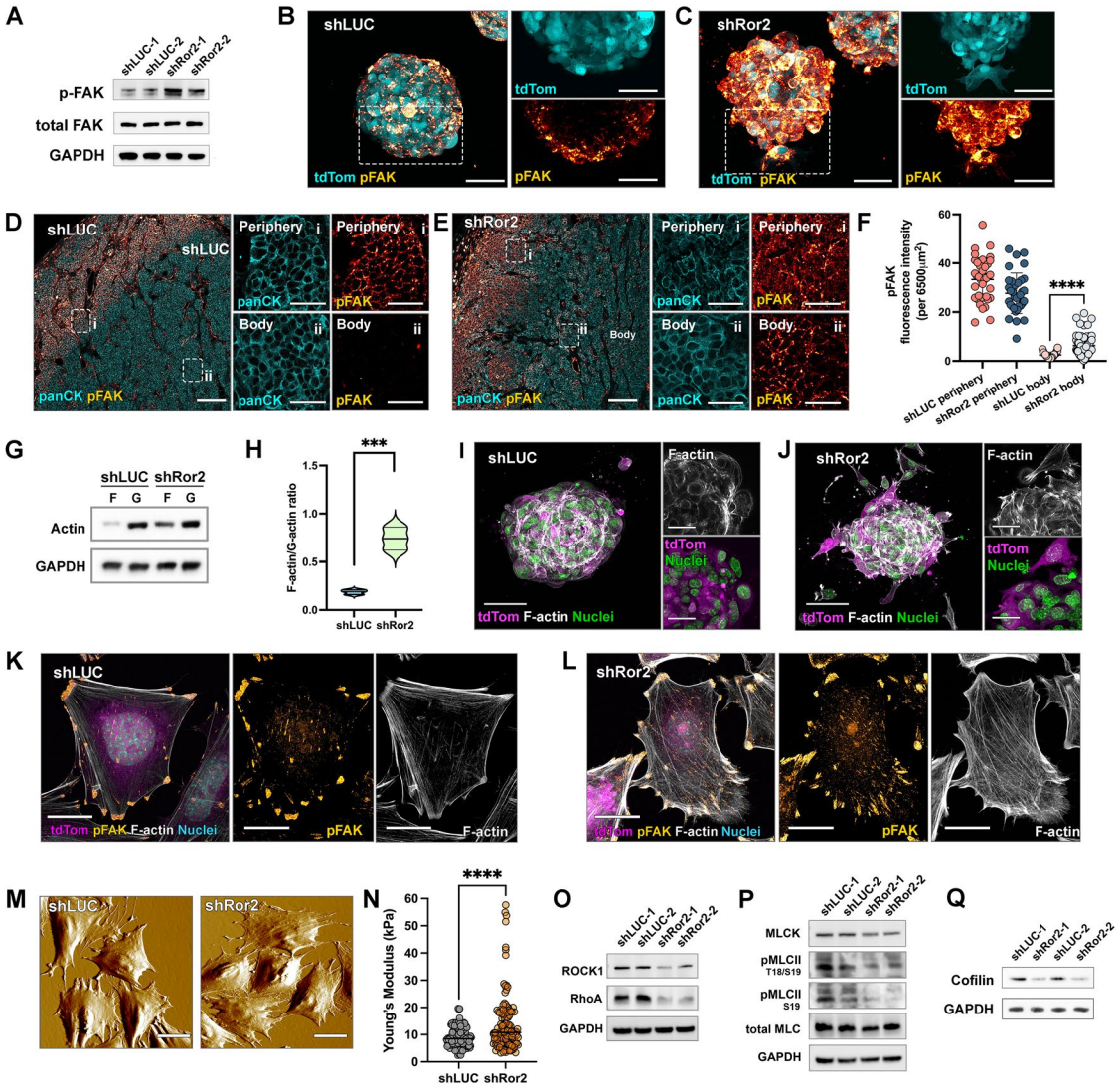

FIGURE 3: Focal adhesions and actin cytoskeleton dynamics are regulated by Ror2. (A) Western blot of 2225L shLUC and shRor2 organoids for phosphorylated FAK (Y861) and total FAK showing increased FAK phosphorylation in Ror2-depleted organoids. (B, C) Immunofluorescence of pFAK (orange hot LUT) and tdTomato+ tumor cells (cyan) in 2225L organoids, showing an increase in pFAK levels and distribution within protrusions upon (C) Ror2 loss compared with (B) pFAK in shLUC organoids. Boxed insets represent 6 μm cross-section of (B) shLUC and (C) shRor2 organoids. Scale 50 μm. (D) Immunofluorescence of pFAK (orange hot LUT), tdTomato+ tumor cells (cyan) in 2225L shLUC primary tumor sections, showing topographic distribution of pFAK in control tumors. Scale 100 μm. (Di) Prevalent pFAK staining in the periphery of shLUC tumors. (Dii) Limited pFAK staining in the body of shLUC tumors. Inset scale 30 μm. (E) Immunofluorescence of pFAK (orange hot LUT), tdTomato+ tumor cells (cyan) in 2225L shRor2 primary tumor sections, showing topographic alterations in pFAK distribution upon Ror2 loss. Scale 100 μm. (Ei) Prevalent pFAK staining in the periphery of shRor2 tumors. (Eii) Expansion of pFAK staining in the body of shRor2 tumors. Inset scale 30 μm. (F) Quantitation of pFAK immunofluorescence intensity per 6500 mm^2 area, distinguishing between periphery and inner tumor body of shLUC and shRor2 tumors. Statistically significant increase in pFAK fluorescence intensity is shown (****$p < 0.00001$, $n = 3$–4 tumors per group, ≥10 regions within periphery and body per tumor evaluated). (G) F-actin/G-actin ratio assay of 2225L shLUC and shRor2 cells showing increased F-actin content in Ror2-depleted cells. (H) Quantification of the F-actin/G-actin ratio in 2225L shLUC and shRor2 cells (***$p < 0.0001$; $n = 3$ biological replicates). (I, J) Immunofluorescence for F-actin (Spy650 FastAct, gray), tdTomato+ tumor cells (magenta), and nuclei (green) in (I) shLUC and (J) shRor2 organoids, depicting cortical localization of F-actin in shLUC vs. (J) formation of F-actin stress fibers in shRor2 organoids, particularly around areas of invasion into the ECM. Scale 75 μm, inset scale 25 μm. (K, L) 2D immunofluorescence of F-actin (SpyNuc 650, gray), pFAK (orange hot LUT), and nuclei (cyan) in (K) shLUC vs. (L) shRor2 organoids. Scale 20 μm. (M) AFM and 3D surface spatial topology of shLUC and shRor2 cells in monolayer. Scale 30 μm. (N) Quantitation of elasticity, or Young's modulus, across shLUC and shRor2 cells. Young's modulus means, 2225L shLUC 8.0 ± 3.5 kPa vs. shRor2 14.0 ± 10.4 kPa. (O) Western blotting for ROCK1 and RhoA, along with GAPDH internal control. (P) Western blot for MLCK, pMLCII, and total MLC. (Q) Western blot of 2225L shLUC and shRor2 organoids for cofilin showing reduced cofilin expression in Ror2-depleted organoids.

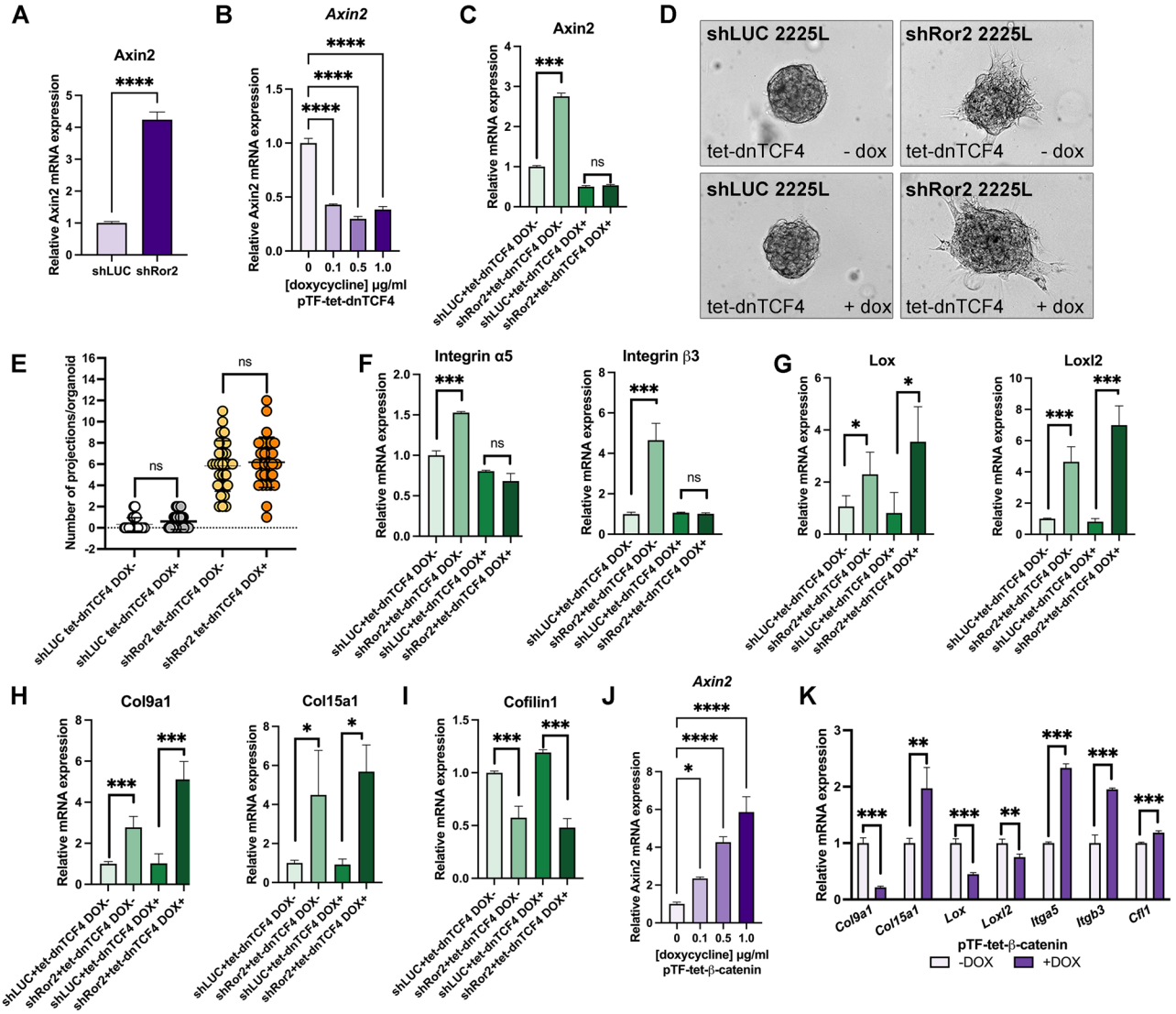

FIGURE 4: Wnt/Ror2 and Wnt/β-catenin pathways differentially regulate ECM composition and cell–ECM interactions during tumor cell invasion. (A) RT-qPCR for *Axin2* in shLUC vs. shRor2 organoids demonstrating that Wnt/β-catenin signaling is induced upon Ror2 depletion in 2225L tumor cells. (B) RT-qPCR for *Axin2* after 72 h post–doxycycline induction of a pTF-tet-dnTCF4 lentiviral construct in 2225L tumor cells to block Wnt/β-catenin signaling. Shown is a dose-dependent inhibition of *Axin2* upon dnTCF4 induction. (C) RT-qPCR for *Axin2* after 72 h post–doxycycline induction of a pTF-tet-dnTCF4 lentiviral construct in shLUC and shRor2 2225L tumor cells showing the inhibition of *Axin 2* expression upon Ror2 loss and dnTCF4 induction. (D) Brightfield DIC images of shLUC and shRor2 organoids in the presence or absence of dnTCF4 induction. Shown are representative images after 3 d of culture post–dnTCF4 induction. (E) Quantitation of invasion in shRor2 vs. shLUC organoids after blocking Wnt/β-catenin signaling by dnTCF4. ($n = 30$ organoids per group, representing three independent experiments). (F–I) RT-qPCR for ECM-associated genes in shLUC vs. shRor2 tumor cells upon dnTCF4 induction, including (F) *α5 integrin* and *β3 integrin,* (G) *Lox* and *Loxl2,* (H) *Col9a1* and *Col15a1,* (I) *Cofilin 1*. (J, K) Inducible expression of β-catenin within 2225L tumor cells and RT-qPCR for (J) *Axin2* induction following dose-dependent administration of doxycycline for 72 h and (K) RT-qPCR of ECM-associated genes *Col9a1, Col15a1, Lox, Loxl2, Itga5, Itgb3,* and *Cfl1* showing different outcomes following β-catenin induction compared with Wnt/Ror2 impairment. (A–K) ****$p < 0.0001$, ***$p < 0.001$, **$p < 0.01$, *$p < 0.05$.

While pERM was located at the cell cortex of shLUC tumor cells, a discontinuous punctate localization of pERM was prevalent in shRor2 tumor cells (Supplemental Figure S2C′, arrows), likely reflecting altered intercellular and cell–ECM interactions. These data collectively demonstrate a role for Wnt/Ror2 status in dictating pericellular ECM composition and integrin signaling, the outcome of which shapes the formation of focal adhesions, actin cytoskeletal changes, and the transmission of ECM-derived signals necessary for cancer invasion.

Wnt/Ror2 and Wnt/β-catenin pathways differentially regulate tumor cell–ECM exchanges during invasion

Wnt/Ror2 signaling can repress Wnt/β-catenin signaling depending on the cellular context. The spatial segregation of Wnt/β-catenin active versus Wnt/Ror2 subpopulations in vivo prompted us to assess the contribution of heightened Wnt/β-catenin activity observed upon Ror2 LOF (van Amerongen *et al.*, 2012; Roarty *et al.*, 2015, 2017). We confirmed an increase in Wnt/β-catenin signaling activity, assessed by the induction of the downstream negative feedback

regulator *Axin2*, upon Ror2 knockdown within TP53-null 2225L tumor cells (Figure 4A). We next tested Wnt/β-catenin LOF in the context of Ror2 depletion by conditionally overexpressing a dominant negative form of TCF4. We confirmed that induction of dnTCF4 reduced *Axin2* expression in a dose-dependent manner and, moreover, suppressed the elevated Wnt/β-catenin–dependent *Axin2* expression brought about by Ror2 depletion (Figure 4, B and C). We then determined the contribution of Wnt activation to the invasion of tumor cells. Interestingly, Wnt/β-catenin LOF did not impede invasion prompted by Ror2 knockdown, suggesting that the dissemination of tumor cells results from impaired Wnt/Ror2 signaling and not the derepression of Wnt/β-catenin signaling in this context (Figure 4, D and E). We additionally assessed ECM-associated gene expression changes that occurred upon Wnt/β-catenin LOF in shLUC and shRor2 organoids. We determined that Wnt/β-catenin LOF impaired integrin up-regulation (*Itga5, Itgb3*) upon Ror2 loss but was dispensable for the deposition of tumor cell–intrinsic ECM production (*Col9a1, Col15a1*) and expression of Lox family enzymes downstream of Wnt/Ror2 signal loss (Figure 4, F–H). Moreover, inducible activation of Wnt/β-catenin alone in tumor cells elicited distinct effects as compared with Wnt/Ror2 on EMT- and ECM-associated gene networks (Figure 4, J and K; Supplemental Figure S3, B and C), where Wnt/β-catenin activation prompted the up-regulation of mesenchymal genes despite the inability to alter ECM composition. These data suggest that Ror2 LOF phenotypes in this context are not a consequence of ectopic Wnt/β-catenin activation (Roarty *et al.*, 2017). These findings suggest that a balance of Wnt/Ror2 and Wnt/β-catenin signaling outputs differentially impacts cadherin-based adhesions, EMT, and integrin–ECM interactions to provide specific spatiotemporal regulation of cell adhesive and invasive behaviors for tumor cells during cancer progression.

Inhibition of integrin and FAK impedes directional migration prompted by Ror2 loss

To determine the functional necessity of integrin and FAK activation on Ror2 LOF phenotypes with respect to invasion and dissemination, we tested small molecular inhibitors of both integrin and FAK activation. ATN-16, a novel small molecule peptide antagonist of $\alpha_5\beta1$ integrin, successfully inhibited pFAK activation induced by Ror2 loss in a dose-dependent manner (Figure 5, A and D). We subjected 2225L TP53-null 2D cells to an in vitro invasion assay to test the effect of ATN-161 (10 μM) on the ability of shRor2 cells to efficiently invade into a cell-free gap created within the tumor cell monolayer. After 16 h, shRor2 cells were more efficient at filling the gap than control shLUC cells; however, ATN-161 resulted in a significantly greater impairment of Ror2-deficient cell migration and wound closure than shLUC control cells (Figure 5, B and C). The inhibitor PF-562271 besylate, a potent ATP-competitive reversible inhibitor of FAK activation, was also tested given the elevated pFAK levels in both in vitro organoids and in vivo tumors upon Ror2 loss. Treatment with PF-562271 successfully mitigated the activation of FAK phosphorylation upon Ror2 depletion (Figure 5, E and H). Moreover, migration of shRor2 tumor cells was greatly reduced upon PF-562271 treatment in 2D wound healing assays (Figure 5, F and G). Such a reduction in migration and invasion was additionally observed in 3D organoid cultures, which represent a more physiologically relevant cell–ECM landscape (Figure 5, I–N). With either $\alpha_5\beta1$ integrin inhibition with ATN-161 (Figure 5, J and K) or pFAK inhibition with PF-562271 (Figure 5, M and N), both the number of invasive protrusions and the extent of invasion, as measured by distance of tumor cell dissemination, upon Ror2 loss were significantly reduced. Thus, these results place integrin-mediated signaling and FAK activation downstream of Wnt/Ror2 signaling and support a model where tumor cell movements and actin cytoskeletal remodeling are shaped by Ror2-mediated, cadherin-based intercellular adhesions and integrin-based focal adhesions within the tumor microenvironment. These findings have important implications for the regulation of tumor cell–ECM behaviors downstream of Wnt/Ror2 signaling, governing decisions of cell adhesion, invasion, and survival during breast cancer metastasis.

DISCUSSION

Cancer cells exhibit extremely adaptable cellular programs enabling their successful dissemination, survival, transit, and establishment of distant metastases. Such proficiency in migration and invasion mechanisms requires extensive cell–cell and cell–ECM exchanges along with molecular signaling events that guide and mobilize tumor cells. We demonstrate that the noncanonical Wnt receptor, Ror2, regulates intercellular adhesion and cell–ECM interactions impacting tumor cell invasion and ECM composition to facilitate cancer cell invasion. We discovered that compromised Wnt/Ror2 signaling in vivo and within 3D-cultured tumor organoids specifically disrupts actin dynamics, adhesion, and tumor cell–intrinsic ECM deposition, including collagen cross-linking gene expression programs likely conducive for reinforcing tumor cell transit from the primary tumor. Interestingly, E-cadherin down-regulation was observed upon Ror2 loss, particularly at invading tumor cell protrusions within the surrounding ECM (Figure 1). Integrin receptors, specifically α_5 integrin and β_3 integrin, were also up-regulated around the invasive front and cell–matrix interface of Ror2-deficient tumor cells within in vitro organoids and in vivo (Figure 2). Similar spatial changes in integrins and their roles in maintenance of directional migration exist in prostate cancer cells (Joshi *et al.*, 2017) and fibroblasts (Gopal *et al.*, 2017; Missirlis *et al.*, 2017), as well as developmental processes encompassing convergent extension and oriented cell division (Dohn *et al.*, 2013; Parisi *et al.*, 2020). This change in integrin presence and clustering was also accompanied by the simultaneous production of a provisional fibronectin matrix upon Ror2 loss, a vital component of the ECM, ligand for α5 integrin, and mediator of collagen assembly and organization (Vega and Schwarzbauer, 2016). Along with altered ECM architecture, Ror2 down-regulation changed the intratumor spatial landscape of integrin and FAK activation within primary tumors (Figures 2 and 3), conveying an important physiological function for Ror2 in shaping both signaling and ECM architecture during tumor progression. This change in FAK activation and F-actin dynamics was accompanied by a decrease in elasticity of shRor2 tumor cells relative to control shLUC tumor cells (Figure 3). Moreover, blocking either integrin, the ECM-associated receptor, or FAK, a downstream mediator of integrin-mediated signal transduction, hindered the migration and dissemination observed upon Ror2 depletion (Figure 5).

The precise cellular and molecular mechanisms regulating tumor cell invasion and dissemination during metastasis remain to be elucidated. EMT has gained considerable attention as a mediator of cancer cell migration, particularly through the binary loss of adherens junction components (E-cadherin) and tight junctions (claudins) and up-regulation of mesenchymal transcription factors Snail, Twist, and Zeb1 (Miettinen *et al.*, 1994; Nieto *et al.*, 2016). However, emerging evidence now demonstrates that collective cell migration likely also contributes to invasion and metastasis in cancer (Cheung *et al.*, 2013; Bronsert *et al.*, 2014; Williams *et al.*, 2019). Like normal developmental contexts where the biological process is building a tissue or healing a wound, tumors also encompass cell-rich environments that range in form and function (Friedl and Gilmour, 2009).

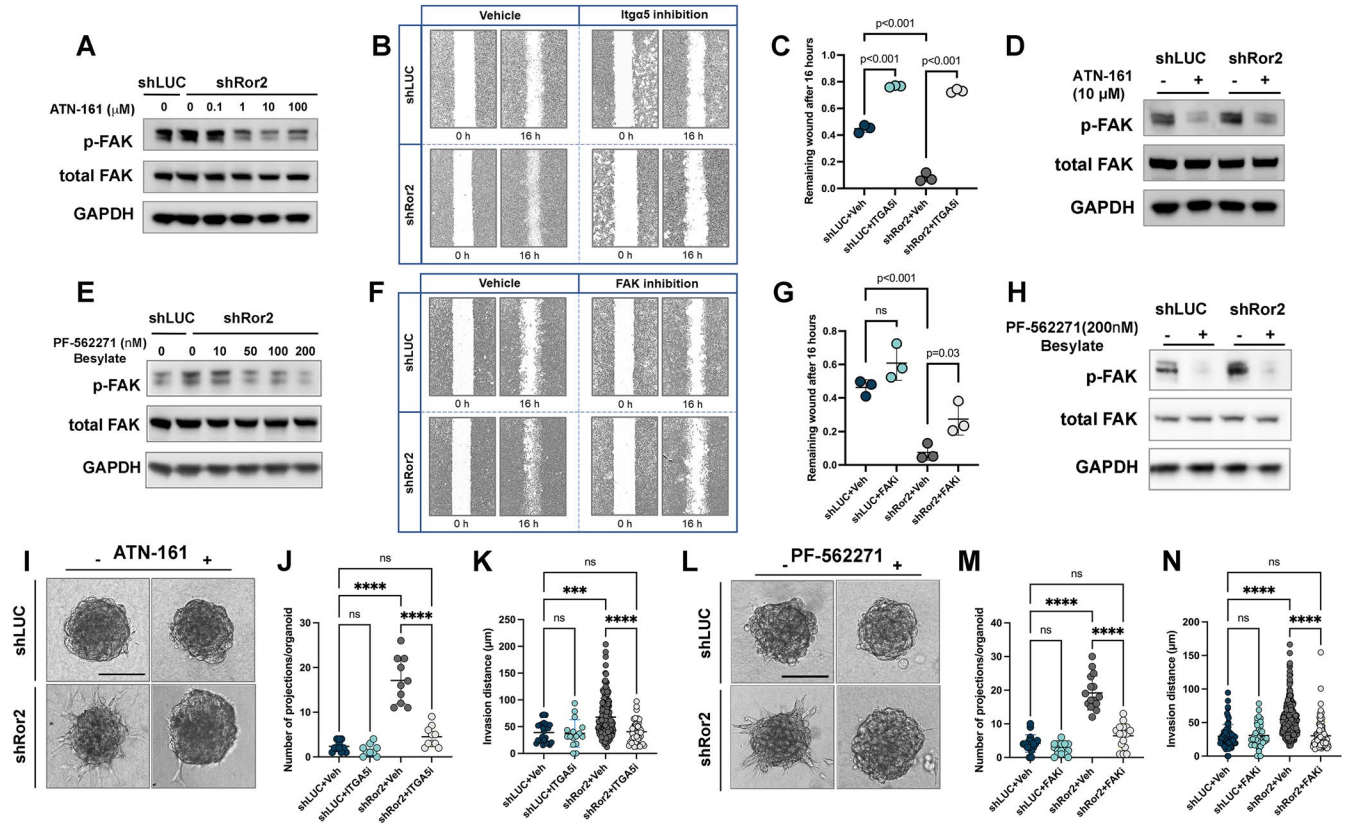

FIGURE 5: Inhibition of α_5 integrin or FAK inhibit breast cancer cell migration and invasion downstream of Ror2 loss. (A) Western blot of 2225L shLUC and shRor2 cells for phosphorylated FAK and total FAK after 0, 0.1, 1, 10, or 100 μM ATN-161 treatment. (B) Brightfield images of wound healing assays on 2225L shLUC and shRor2 cells with or without integrin α_5 inhibition (10 μM ATN-161) showing cell migration within 16 h. (C) Quantification of the ratio of remaining wound area after 16 h to the initial wound area with or without integrin α_5 inhibition. (D) Western blot of 2225L shLUC and shRor2 organoids for phosphorylated FAK and total FAK after 10 μM ATN-161 treatment. (E) Western blot of 2225L shLUC and shRor2 cells for phosphorylated FAK and total FAK after 0, 10, 50, 100, or 200 nM PF-562271 besylate treatment. (F) Brightfield images of wound healing assays on 2225L shLUC and shRor2 cells with or without FAK inhibition (200 nM PF-562271 besylate) showing cell migration within 16 h. (G) Quantification of the ratio of remaining wound area after 16 h to the initial wound area with or without FAK inhibition. (H) Western blot of 2225L shLUC and shRor2 organoids for phosphorylated FAK and total FAK after 200 nM PF-562271 besylate treatment. (I) Brightfield DIC images showing compromised invasion of shRor2 organoids into the surrounding matrix after integrin α_5 inhibition. Scale 30 μm. (J) Quantitation of cellular projections emanating into the surrounding matrix in shRor2 vs. shLUC organoids (****$p < 0.0001$, ***$p < 0.001$; ns: not significant). (K) Quantitation of invasion distance per invasive projection within shLUC and shRor2 organoids after Itga5 inhibition. shLUC+veh 39.05 ± 18.78 μm, shLUC+ITGA5i 37.43 ± 25.58 μm, shRor2+veh 67.74 ± 35.26 μm vs. shRor2+ITGA5i 40.53 ± 21.0 μm (****$p < 0.0001$, ***$p < 0.001$; ns: not significant). (L) Brightfield DIC images showing compromised invasion of shRor2 organoids into the surrounding matrix after integrin α_5 inhibition. Scale 30 μm. (M) Quantitation of cellular projections emanating into the surrounding matrix in shRor2 vs. shLUC organoids after FAK inhibition (****$p < 0.0001$, ***$p < 0.001$; ns: not significant). (N) Quantitation of invasion distance per invasive projection within shLUC and shRor2 organoids after FAK inhibition. shLUC+veh 29.56 ± 17.31 μm, shLUC+FAKi 30.74 ± 23.8 μm, shRor2+veh 54.54 ± 23.8 μm vs. shRor2+FAKi 30.3 ± 20.5 μm (****$p < 0.0001$, ***$p < 0.001$; ns: not significant). For invasive distance, 50–200 invasive projections were measured using the ImageJ line tool per condition, representing a minimum of 30 organoids per group.

Detailed analysis of the EMT process has helped define mechanisms responsible for cancer progression, particularly aspects of cellular plasticity, treatment resistance, and intermediary cell states during cancer cell adaptation and tumor evolution (Mani *et al.*, 2008; Grigore *et al.*, 2016; Nieto *et al.*, 2016). Nonetheless, defining the regulation of specific cell–cell and cell–ECM interactions during tumor progression is a necessary step to understand the interplay of cell signals guiding multicellular tumor cell behaviors. In the present study, we establish that depletion of Ror2 levels in tumor cells disrupts the level and localization of E-cadherin within tumor cell junctions (Figure 1). Although we occasionally observed the concomitant expression of the mesenchymal marker, vimentin, in invasive areas associated with E-cadherin loss, we did not observe the overt up-regulation of mesenchymal genes in shRor2 organoids, suggesting that the down-regulation of junctional E-cadherin predominantly occurred in the absence of a distinct mesenchymal switch after Ror2 down-regulation. This observation has important implications in cancer cell invasion and metastatic progression given that fluctuations in E-cadherin levels, dictated by Ror2, might play an essential role in dictating states of cell adhesion, dissemination, and survival during metastatic progression (Onder *et al.*, 2008; Padmanaban *et al.*, 2019). Importantly, E-cadherin levels are diminished but not

completely lost upon Wnt/Ror2 disruption. This type of hybrid EMT state, rather than a complete mesenchymal state, is associated with tumor cell aggression in metastasis (Kroger *et al.*, 2019; Luond *et al.*, 2021; Pastushenko *et al.*, 2021; Grasset *et al.*, 2022). Beyond E-cadherin as a marker of the epithelial state in EMT, roles for E-cadherin include the regulation of epithelial organization and polarity (Takeichi, 1991), as well as the modulation of growth factor signals like EGF (Hoschuetzky *et al.*, 1994; Qian *et al.*, 2004). In line with such roles for E-cadherin, the regulation of junctional mechanocoupling by Wnt5a/Ror2 has been observed during angiogenic collective migration, where Wnt5a activated Cdc42 at cell junctions and stabilized vinculin/α-catenin binding to support adherens junction coupling with the actin cytoskeleton (Carvalho *et al.*, 2019). Interestingly, vinculin levels were up-regulated as a consequence of Ror2 deletion in our models based on RNA sequencing (Figure 2), suggesting potential compensatory mechanisms in response to E-cadherin loss and altered mechanoregulation of cell–cell adhesion in tumor cells (le Duc *et al.*, 2010). Nonetheless, cellular and microenvironmental contexts likely shape Ror2 signaling and its functions in vitro and in vivo. Contrasting tumor suppressive and tumor promoting roles have been ascribed to Wnt/Ror2 signaling in breast cancer (Bleckmann *et al.*, 2016; Roarty *et al.*, 2017; Guo *et al.*, 2020; Menck *et al.*, 2021), and factors like cellular heterogeneity, receptor/ligand context, cellular cross-talk, and the multistep nature of cancer metastasis likely contribute to the complexity of the Wnt signaling function in cancer, much like TGF-β and its known pleiotropic functions (Bierie and Moses, 2006). For instance, in melanoma, changes in cell and microenvironment contexts are integral in shaping different cellular phenotypes dictated by Wnt5a, a key ligand for Ror2, in primary and metastatic settings (Fane *et al.*, 2022).

The alteration in tumor stroma, particularly the increased presence of type I collagen upon Wnt/Ror2 disruption (Figure 1), prompted our investigation of Wnt/Ror2 signaling in controlling cell–cell and cell–matrix interactions in TNBC. Increased ECM stiffness within the tumor microenvironment is associated with poor patient prognosis across breast and other cancer types (Colpaert *et al.*, 2003; Levental *et al.*, 2009; Conklin *et al.*, 2011). Enhanced cross-linked collagen within the ECM milieu contributes to ECM stiffness, promoting tumor cell invasion and metastasis (Spill *et al.*, 2016). Our data now suggest that ECM composition and tumor cell phenotype are shaped by cell intrinsic spatiotemporal Wnt modes of signaling within the tumor landscape. In addition to the reinforcement of collagen cross-linkers within the lysyl oxidase gene family (lox, loxl2; Figure 1), the heightened integrin expression upon Ror2 loss, particularly α_5 and β_3 integrins, prompted us to investigate the composition and reinforcement of ECM cues that enabled Ror2-deficient tumor cells to migrate and invade. Fibronectin is a known structural ECM protein that binds α5 integrin, and its polymerization is known to regulate the composition and stability of extracellular matrix fibrils, particularly type I collagen (Sottile and Hocking, 2002; Kadler *et al.*, 2008). Intriguingly, we not only detected the clustering and up-regulation of α5 integrin at sites of tumor cell invasion, but we also detected the tumor cell–intrinsic deposition of fibronectin upon Ror2 depletion, prevalent in areas of active invasion into the surrounding collagenous ECM (Figure 2). This observation was observed in vitro within organoids and in vivo within tumors. Interestingly, while dnTCF4-mediated inhibition of β-catenin activation did not impact tumor cell invasion prompted by Ror2 loss, β-catenin–dependent signaling in the absence of Ror2 contributed to the up-regulation of *Itga5* and *Itgb3* (Figure 4). Moreover, β-catenin–dependent effects on tumor cells were distinct from Wnt/Ror2 disruption with respect to collagen cross-linking, matrix deposition and composition, and actin cytoskeleton changes, suggesting that Wnt/β-catenin–dependent and Wnt/Ror2 signaling differentially modulate ECM ligand-receptor repertoires to shape tumor cell adhesion and invasion. Wnt signaling has been implicated in the setting of fibrosis and wound healing (Bielefeld *et al.*, 2011; Kumawat *et al.*, 2013; Wehner *et al.*, 2017), yet it remains unclear how spatiotemporal control of cell–ECM interactions is achieved by distinct, but integrated, modes of Wnt signaling across a multicellular context. Our studies have several implications for tumor progression, specifically where the integration of Wnt signaling modes is present among subpopulations within the cell-rich landscape of TNBC (Roarty *et al.*, 2017).

Our results may help explain how fibronectin expression, guided by Ror2 presence, provides key signals for tumor cells to survive, directionally orient, and move through the local microenvironment to invade and eventually disseminate from the primary tumor (Gopal *et al.*, 2017). Key studies in *Xenopus* demonstrate that integrin–fibronectin interactions can specifically polarize actin-rich protrusions, and such protrusive activity exerted by migrating cells subsequently helps to fuel polymerization and orientation of ECM fibrils through tractional forces generated by the migrating cell (Boucaut and Darribere, 1983; Alfandari *et al.*, 2003; Davidson *et al.*, 2008). Moreover, given that a polymerized fibronectin network is also important for the assembly of other ECM-associated constituents like collagens (Sottile and Hocking, 2002), heparin sulfate proteoglycans (Heremans *et al.*, 1990), and tenascin C (Van Obberghen-Schilling *et al.*, 2011), our results place Wnt/Ror2 signaling as an important nexus for tumor cell exchanges with the ECM. Ror2 down-modulation in vivo drastically augmented the integrin, collagen, and fibronectin presence within tumor cells and changed the topology of cell–ECM signaling in vivo such that focal adhesion activation was expanded in Ror2-depleted versus Ror2-intact tumors (Figures 1–3). Interestingly, matrix rigidity has been shown to impact the amplitude of Wnt/β-catenin activity through down-modulation of the negative regulator Dikkopf-1 (Dkk1) (Barbolina *et al.*, 2013). Whether such feedback mechanisms apply in our studies remains an open question. Integrins are critical ECM receptors that relay extracellular signals to receiving cells, and their content and activity can dictate reciprocal cell–ECM responses during malignancy (Levental *et al.*, 2009). The fact that integrins, fibronectin, and other ECM components, identified downstream of Wnt/Ror2 signaling in this study, have been implicated in the regulation of tumor cell dormancy and survival during cancer metastasis (Ghajar *et al.*, 2013; Osmani *et al.*, 2019; Barney *et al.*, 2020) warrants further investigation. These data, together with other studies that demonstrate that fibronectin can promote directional persistence of cancer cell invasion (Erdogan *et al.*, 2017), suggest that alternative Wnt/Ror2 signaling orchestrates critical tumor cell–ECM interactions within TNBC by elaborating matrix composition and specific interactions between the cancer cell and its microenvironment.

Aside from Wnt/β-catenin signaling, Wnt/PCP signaling through Wnt/Glipican4/Frizzled has been shown to regulate ECM assembly through effects on cadherin-mediated cell cohesion (Dohn *et al.*, 2013). VANGL/Prickl1a have opposing functions on ECM organization with respect to fibronectin assembly in zebrafish embryos. Other studies have implicated Wnt/PCP as an essential mediator of integrin transmission of cytoskeletal tension required to direct fibronectin fibril formation at cell surfaces during convergent extension in *Xenopus* embryos (Dzamba *et al.*, 2009). The down-regulation of cofilin and shift in F-actin/G-actin ratios upon Ror2 loss suggest that Wnt/Ror2 signaling is an important determinant for tumor cell–intrinsic ECM production and response by modulating actin polymerization and depolymerization. Roles for cofilin in migration and turning of

metastatic cancer cells exist, highlighting the rather intricate functions such proteins perform in directing deliberate tumor cell movements (Sidani *et al.*, 2007). Known roles also exist for Wnt signaling in reorganizing the actin cytoskeleton in various developmental and cancer contexts across metazoans, particularly though Rho GTPase interactions (Lai *et al.*, 2009; Schlessinger *et al.*, 2009). Interestingly, during zebrafish gastrulation, Wnt11 controls tissue morphogenesis by modulating E-cadherin–mediated cell cohesion through Rab5c-dependent actin remodeling (Ulrich *et al.*, 2005).

Based on these observations, critical questions remain of how the spatial integration and interplay of Wnt pathways regulate cellular diversity and tumor cell behavior during cancer progression. Given our previous findings that canonical and noncanonical Wnt signaling modes are integrated within mammary development and breast cancer (Kouros-Mehr and Werb, 2006; Roarty *et al.*, 2015, 2017), the characterization of Wnt/Ror2 and other Wnt signaling modes in shaping the evolutionary landscape of tumor cells during breast cancer metastasis will be of interest. Defining such signaling pathways that shape adhesive, migratory, and survival states within a tumor will provide a more comprehensive understanding of the phenotypic variation of tumor cells and the spatiotemporal states of signaling guiding both the composition and cooperativity of cell–ECM interactions during breast cancer progression.

MATERIALS AND METHODS

Request a protocol through *Bio-protocol*.

Mouse strains

This study is compliant with the rules of the Guide for the Care and Use of Laboratory Animals of the National Institutes of Health. The animal maintenance and procedures are approved by the Baylor College of Medicine Institutional Animal Care and Use Committee (Protocol AN-504). A transplantable TP53-null mammary tumor bank was generated as described (Jerry *et al.*, 2000). Basal-like 2225L and 2153L models, maintained as a transplantable biobank, were propagated in the BALB/c inbred female mice (strain #047; 3–4 wk of age; ENVIGO Houston, TX).

Generation of lentiviral constructs

Lentiviral LeGO plasmids encoding shLUC and Ror2 shRNA hairpin antisense sequences are as follows: shLUC, 5′-ATTCCAATTCAGCGGGGGC3′; shRor2-1, 5′-TATTCTGCGTAAAGCACCACG-3′; and shRor2-2, 5′-ATGAGTTTGTAGTAATCTGCG-3′. Clones were sequence validated. shRor2-1 and shRor2-2 hairpin sequences correspond to shRor2-94 and -98 clones from the MISSION pLKO Lentiviral shRNA libraries (Sigma). Wnt pathway reporters (plasmid 7TGC #24304; Addgene, Cambridge, MA) were validated in mammary epithelial cells as described (Roarty *et al.*, 2015, 2017). For dnTCF4 (pCWXPGR-pTF-dnTCF4; plasmid #114277) and β-catenin (pCWX-PGR-pTF-betaCatenin; plasmid #114281) lentiviral studies, plasmids were a gift from Patrick Salmon (University of Geneva Medical School, Geneva, Switzerland) and acquired from Addgene.

Tumor cell isolation

Tumor tissues were minced into 1 × 1 mm fragments and enzymatically dissociated in hanks balanced salt solution (HBSS) containing 1 mg/ml collagenase A (#11088793001; Roche, Basel, Switzerland) and 1 µg/ml DNase I (#07900; StemCell Technologies, Vancouver, Canada) in a shaking incubator at 37°C, rotating at 125 rpm for 2 h. Tissue digests were mixed every 20 min with gentle pipetting to facilitate homogeneous dissociation. To enrich for tumor organoids, digests were subjected to differential centrifugation at 1500 rpm for 10 s, repeating three times. Enriched organoids were further dissociated using TrypLE at 37°C for 5 min and filtered through a 40 µm cell strainer to obtain single cells. Single cells were washed with 1× phosphate-buffered saline (PBS) and resuspended in culture media for lentiviral transduction. The composition of growth media included DMEM/F-12 (#11320033; ThermoFisher Scientific, Waltham, MA) supplemented with 10% fetal bovine serum (FBS) (#10082147; ThermoFisher Scientific), 5 µg/ml insulin (#I5500; Sigma-Aldrich, St. Louis, MO), 1 µg/ml hydrocortisone (#H0888; Sigma-Aldrich), and 10 ng/ml mEGF (#SRP3196; Sigma-Aldrich). Geneticin (200 µg/ml) (#10131035; ThermoFisher Scientific) was added to select for TP53-/- tumor cells based on the Neo cassette retained within the original knockout mouse model. For organoid cultures, single cells (500,000 cells/well) were seeded and transduced in ultra–low attachment 24-well plates (#3473; Corning, Corning, NY) to enable the simultaneous transduction and formation of cell aggregates. Aggregated organoids were then embedded within matrices for tumor organoid assays.

Lentiviral transduction of tumor cells for in vitro and in vivo studies

For organoid studies and propagation of lentiviral-transduced tumors, primary tumor cells (500,000 cells/well) were infected overnight (16 h) in ultra–low attachment 24-well plates in suspension at a multiplicity of infection (MOI) of 30 with lentivirus in growth media. Cells were briefly rinsed three times with PBS after overnight infection and then used in the subsequent studies. For 2D infection of monolayer cultures, tumor cells were seeded at a density of 100,000 cells per well of six-well culture plates (#CLS3516; Corning, Corning, NY) and infected at an MOI of 30 with lentivirus in culture media. Cells were briefly rinsed three times with PBS after overnight infection and then expanded for subsequent studies. For in vivo studies, transduced tumor cells in suspension were resuspended in a 1:1 ratio of growth factor–reduced Matrigel/HBSS at 25,000 cells/10 µl injection volume. Tumor cells were injected into cleared #4 inguinal mammary fat pad of BALB/c inbred female mice (strain #047; 3–4 wk of age; ENVIGO, Houston, TX). Tumors were collected when they reached a diameter of 1 cm or volume of 500 mm^3.

Tumor organoid assays

Organoid assays were performed within 3D neutralized type I collagen matrices at a concentration of 2 mg/ml. Rat-tail collagen type I (#50201; Ibidi) was diluted in 10× MEM, sterile dH_2O, and 7.5% sodium bicarbonate solution to achieve a neutralized 2 mg/ml collagen solution at pH 7.0. Eight-well chamber slides were coated with 5 µl of neutralized collagen and incubated at 37°C for 15 min. Preassembled organoids from overnight cultures were washed in PBS before being suspended in collagen at 50,000 cells/40 µl volume. A cell suspension (40 µl) was plated into each chamber, and the chamber slides were incubated at 37°C for 1 h. After polymerization, collagen gels were overlaid with 500 µl of growth media. Primary tumor organoids were cultured for 72–96 h and then fixed for histological examination or recovered from the matrices for RNA and protein assessment. For RNA and protein extractions, collagen matrices were dissociated in 2 mg/ml collagenase A solution at 37°C for 20 min under constant rotation at 40 rpm to liberate organoids. Organoids were then washed with 1× PBS and collected by a series of short centrifugation steps before cell lysis.

Processing of tumor tissue and organoid cultures

5-Bromo-2′-deoxyuridine (Brdu) at 60 µg/g body weight was injected into the mice via intraperitoneal injection 2 h before tissue collection. Tumors were dissected and fixed in 4% paraformaldehyde overnight

at 4°C before processing to paraffin blocks. Organoid cultures were washed with PBS and fixed in 4% paraformaldehyde for 10 min at room temperature before being processed to paraffin blocks. Before processing in paraffin block, organoids in 3D collagen were embedded within HistoGel (Epredia; #22-11-678) to help maintain orientation and integrity before processing. Paraffin-embedded tumor tissue or 3D organoids were sectioned at 5 μm thickness before immunostaining.

Immunostaining

Tissue and organoid sections were deparaffinized, rehydrated, and subjected to heat-induced epitope retrieval using sodium citrate, pH 6.0, or Tris-EDTA, pH 9.0, antigen retrieval for 20 min. Sections were blocked at room temperature for 1 h using a commercial M.O.M blocking solution (#BMK-2202; Vector Laboratories, Burlingame, CA) as well as supplementation of 5% bovine serum albumin (BSA). For immunofluorescence staining of 3D organoids in chambered slides, cultures were fixed in 4% paraformaldehyde (PFA) for 15 min at room temperature, washed three times in 1× PBS, permeabilized in 0.05% Triton X-100 for 1 h, washed in 1× PBS, and then blocked (as above) before proceeding to antibody labeling. Primary antibodies were applied overnight at 4°C. Antibodies and concentrations were as follows: Ror2 (1:500; Developmental Studies Hybridoma Bank, Iowa City, IA), eGFP (1:1000; #ab290; Abcam, Cambridge, MA), RFP (1:1000; #600-401-379; Rockland, Pottstown, PA), integrin α_5 (1:1000; #ab150361; Abcam), fibronectin 1 (1:1000; #610077; BD Biosciences, San Jose, CA), phospho-FAK (1:1000; #44-626G; ThermoFisher Scientific), phospho-ERM (1:1000; CST, Danvers, MA), cofilin (1:1000; #5175S; CST), and phospho-cofilin (1:500; #3313S; CST). Sections were washed three times in 1× PBS and incubated with Alexa Fluor 488–conjugated or Alexa Fluor 594–conjugated goat anti-rabbit or anti-mouse immunoglobulin G secondary antibodies in M.OM. diluent containing 5% BSA in the dark for 1 h at room temperature. Sections were washed three times in 1× PBS and counterstained with 1 μg/ml 4′, 6-diamidino-2-phenylindole (DAPI) before mounting slides with ProLong Diamond Antifade Mounting Media (P36961; ThermoFisher Scientific). Tyramide amplification was performed for Ror2 and phospho-FAK detection according to the manufacturer's instructions (#NEL701A001KT; PerkinElmer, Waltham, MA).

Western blotting

Protein samples were separated in NuPAGE 4–12% Bis-Tris protein gels (#NP0336BOX; ThermoFisher Scientific) and transferred to polyvinylidene fluoride membrane (#LC2002; ThermoFisher Scientific) for antibody probing. The blots were blocked with 5% blocker (#1706406; Bio-Rad, Hercules, CA) in Tris-buffer saline containing 0.05% Tween-20. Blots were then incubated with primary antibodies overnight at 4°C before incubating with horseradish peroxidase–conjugated secondary antibodies for 1 h at room temperature. The following antibodies were used in Western blotting: Ror2 (1:1000; Developmental Studies Hybridoma Bank), integrin α_5 (1:1000; #ab150361; Abcam), fibronectin 1 (1:1000; #610077; BD Biosciences), FAK (1:1000; #3285; CST), phospho-FAK (1:1000; #44-626G; ThermoFisher Scientific), ROCK1 (1:1000; #4035; CST), RhoA (1:1000; #2117; CST), cofilin 1 (1:1000; #5175; CST), MLCK (1:1000; #M7905; Sigma-Aldrich), total MLCII (1:1000; #3672; CST), p-MLCII$^{Thr18/Ser19}$ (1:1000; #3674; CST), p-MLCII^{Ser19} (1:1000; #3671; CST), and GAPDH (1:2500; #5174; CST).

F-actin/G-actin assay

Approximately 1×10^7 shLUC and shRor2 cells were harvested. F-actin and G-actin protein samples were collected according to the manufacturer's instructions (#BK037; Cytoskeleton, Denver, CO). F-actin and G-actin were quantified by SDS–PAGE and Western blot using actin antibody (#BK037; Cytoskeleton).

Atomic force microscopy

AFM measurements were conducted at the University of Texas Health Science Center AFM Core Facility at Houston using a BioScope II Controller (Bruker Corporation, Santa Barbara, CA). This system was also integrated to a Nikon TE2000-E inverted optical microscope (Nikon Instruments, Lewisville, TX) to facilitate bright field/fluorescence imaging. 2225L shLUC and shRor2 cells were seeded in collagen (50 μg/ml)-coated 60 mm polystyrene plates to 50% confluence and incubated for 24–48 h at 37°C in a 5% CO_2 atmosphere in growth media. Force curves from at least 20 randomly selected cells per treatment were acquired using Novascan colloidal AFM probes (Novascan Technologies, Boone, IA). These probes consisted of a 5-μm-diameter borosilicate glass particle attached to the edge of a silicon nitride V-shaped cantilever with a nominal spring constant of 0.24 N/m. The cantilever was calibrated for its laser sensitivity using the thermal oscillation method before each experiment. Indentation curves were captured using a 4-μm ramp size, to a scan rate of 0.5 Hz, and a trigger threshold with a maximum load of 10 nN. Young's modulus was calculated following the Hertz model (spherical indenter radius = 2.5 μm) with a Poisson's ratio of 0.5, using NanoScope Analysis software version 3.0 (copyright Bruker Corporation).

To investigate the topography of the cell membrane and the 3D structure of the entire cell, shLUC and shRor2 cells in monolayer were fixed in fresh 4% PFA and rinsed for 10 min in three washes of 1× PBS. Never-dried cells were scanned in 1× PBS using MLCT cantilevers (fo = 4–10 kHz, k = 0.01 N/m, ROC = 20 nm) (Bruker Corporation, Santa Barbara, CA). Cell imaging was performed using contact mode operated in liquid to a scan rate of 0.7 Hz. Images were captured to a scan area of 15–160 μm^2 depending on the cell sizes.

Microscope image acquisition and analysis

Confocal imaging (fixed and time lapse) was carried out within the Optical Imaging and Vital Microscopy Core (OiVM) at Baylor College of Medicine. Incucyte live imaging of 2D wound healing was performed on an IncuCyte S3 system housed within the Integrative Microscopy Core at Baylor College of Medicine. Single-plane or confocal stacks were analyzed using Fiji 1.53c. Confocal imaging of primary tumor sections, organoid sections, or 3D organoids was performed using a Zeiss LSM 880 with Airyscan FAST microscope equipped with a 34-channel spectral array with laser lines at 405, 488, 514, 561, 594, and 633 nm. Leica LSM 880 images were captured with Plan-Apochromat 10×/0.45 (air), Plan-Apochromat 20×/0.8 (air), Plan-Apochromat 40×/1.4 (oil), or Plan-Apochromat 63×/1.4 (oil) objectives. Second harmonic generation microscopy is performed with a Zeiss LSM 780 NLO/2-Photon confocal laser scanning microscope. The 2-Photon features 2NDDs and a Coherent Chamelion Ultra II TiS laser tunable from 690 to 1080 nm. Differential interference contrast (DIC) images of the organoids were captured by a Zeiss Axio Observer A1 microscope with 10× A-Plan/0.25 NA Ph1 and 20× LD-Plan/0.4 NA Ph2 Korr objective lenses. A camera (AxioCam MRm; Carl Zeiss) and digital image acquisition software (AxioVision) were used for DIC images. Immunohistochemistry images were captured by an Olympus BX40 microscope with Olympus UPlanFl 10×/0.3 and UPlanFl 20×/0.5 objectives.

Postprocessing and image analyses were performed in Fiji 2.3.0/1.53q. For measurements of collagen integrated density, color-based thresholding was used to segment the blue regions,

after the Analyze tool was used to measure the integrated density of the blue collagen regions within each tumor. Integrated density is Area (number of pixels) × Total Intensity of pixels. For fluorescence intensity calculations, multiple regions of known area were selected within tumors using the circular draw tool in Fiji. Within the Analyze menu, area integrated intensity and mean gray values were selected for measurement. Background fluorescence was acquired from an area within the specimen lacking fluorescence, and this value was subtracted to arrive at the corrected mean fluorescence intensity.

RNA isolation, sequencing, and analyses

Total RNA was extracted and purified using the RNeasy mini kit following the manufacturer's protocol (#74104; Qiagen, Germantown, MD). The BCM Genomic and RNA Profiling Core performed sample quality checks using the Nanodrop ND-1000 (ThermoFisher Scientific) and a Bioanalyzer Nano chip (Agilent Technologies, Santa Clara, CA). RNA integrity and RNA-seq library preparation were conducted by the Genomics and RNA sequencing Core, followed by Next Gen Sequencing on the NovaSeq 6000 Illumina platform. Following acquisition, postsequencing analysis was conducted by performing sequencing alignment and transcript abundance using STAR or HISAT2 and Cufflinks. Fragment per kilobase of transcript per million mapped reads (Fpkm) values were log2-transformed before analysis, where data were compared to analyze gene expression changes between shLUC and shRor2 groups. Genes were identified as significantly altered in shRor2 conditions based on $p < 0.01$ (*t* test) and fold change cutoff. The Database for Annotation, Visualization and Integrated Discovery (DAVID) was used to help to prioritize gene sets by identifying enriched biological themes, functional-related gene groups, and interacting proteins that were differentially expressed (Huang *et al.*, 2009). RNA sequencing data were deposited in NCBI's Gene Expression Omnibus (GEO) under accession numbers GSE174506 (2225L shLUC vs. shRor2) and GSE176041 (2153L shLUC vs. shRor2) for GEM organoid studies.

Quantitative real-time PCR

Total RNA was reverse transcribed using a high-capacity RNA-to-cDNA kit (#4388950; Applied Biosystems, Foster City, CA). Quantitative real-time PCR (RT-qPCR) was performed by the StepOnePlus Real-Time PCR system using SYBR Green PCR master mix (Applied Biosystems). Primer sequences (Supplemental Table S1) were designed using the NCBI nucleotide BLAST. GAPDH was used as a reference gene for normalization, and relative gene expression fold changes were calculated as $2^{-\Delta\Delta Ct}$.

Wound healing assay

Cells (50,000 cells/well) were seeded into two-well culture inserts (ibidi, Martinsried, Planegg, Germany) in 12-well plates. Medium containing 1% FBS (200 µl) and the indicated vehicle/inhibitors were added to each insert well. Inserts were removed on the following day, and 1 ml of fresh medium containing 1% FBS and the indicated vehicle/inhibitors were added into each well. Live imaging was performed using an IncuCyte S3 system, and the images were analyzed using Wound Healing Tools in Fiji 1.53c (Suarez-Arnedo *et al.*, 2020). The time-lapse movies were generated by Fiji 1.53c.

Statistical analysis and rigor and reproducibility

Data are expressed as the mean ± SD; *n* represents the number of biological replicates, unless specifically indicated otherwise in the figure legends. One-way analysis of variance with Tukey's multiple comparison tests was performed on multigroup comparisons. Unpaired two-tailed Student's *t* tests were performed on analyses involving two-group comparisons unless otherwise noted. Quantitative measurements were performed in ImageJ or GraphPad Prism 9. $p < 0.05$ was considered statistically significant in all analyses, where * $p < 0.05$, ** $p < 0.01$, *** $p < 0.001$, **** $p < 0.0001$). All experiments were reproduced across multiple (≥3) biological replicates.

ACKNOWLEDGMENTS

K. R. is supported by National Cancer Institute (NCI) Transition Career Development Award 5K22CA207463, Susan G. Komen CCR18548284, a Dan L. Duncan Comprehensive Cancer Center Faculty Scholar Award, the L. E Gordon Cancer Research Fund, the Caroline Wiess Law Fund for Research in Molecular Medicine, and NCI Breast SPORE Career Enhancement Award 2P50CA186784. H. S. and N. Z. were additionally supported by CA016303-45 and CA148761-11, respectively, from the National Cancer Institute. We thank Fengju Chen for bioinformatics support within the Biostatistics and Cancer Bioinformatics Division of the Dan L. Duncan Comprehensive Cancer Center. This project was also supported by the Genomic and RNA Profiling Core at the Baylor College of Medicine and the Cytometry and Cell Sorting Core at the Baylor College of Medicine with funding from Cancer Prevention and Research Institute of Texas (CPRIT) Core Facility Support Award CPRIT-RP180672 and National Institutes of Health (NIH) grants P30 CA125123 and S10 RR024574. Imaging for this project was supported by the Optical Imaging & Vital Microscopy (OiVM) core, the Integrated Microscopy Core, and the Center for Advanced Microscopy and Image Informatics (CAMII) at the Baylor College of Medicine with funding from the NIH (DK56338, CA125123, ES030285) and CPRIT (RP150578, RP170719).

REFERENCES

Alfandari D, Cousin H, Gaultier A, Hoffstrom BG, DeSimone DW (2003). Integrin alpha5beta1 supports the migration of Xenopus cranial neural crest on fibronectin. Dev Biol 260, 449–464.

Angers S, Moon RT (2009). Proximal events in Wnt signal transduction. Nat Rev Mol Cell Biol 10, 468–477.

Barbolina MV, Liu Y, Gurler H, Kim M, Kajdacsy-Balla AA, Rooper L, Shepard J, Weiss M, Shea LD, Penzes P, *et al.* (2013). Matrix rigidity activates Wnt signaling through down-regulation of Dickkopf-1 protein. J Biol Chem 288, 141–151.

Barney LE, Hall CL, Schwartz AD, Parks AN, Sparages C, Galarza S, Platt MO, Mercurio AM, Peyton SR (2020). Tumor cell-organized fibronectin maintenance of a dormant breast cancer population. Sci Adv 6, eaaz4157.

Bielefeld KA, Amini-Nik S, Whetstone H, Poon R, Youn A, Wang J, Alman BA (2011). Fibronectin and beta-catenin act in a regulatory loop in dermal fibroblasts to modulate cutaneous healing. J Biol Chem 286, 27687–27697.

Bierie B, Moses HL (2006). Tumour microenvironment: TGFbeta: the molecular Jekyll and Hyde of cancer. Nat Rev Cancer 6, 506–520.

Bleckmann A, Conradi LC, Menck K, Schmick NA, Schubert A, Rietkotter E, Arackal J, Middel P, Schambony A, Liersch T, *et al.* (2016). Beta-catenin-independent WNT signaling and Ki67 in contrast to the estrogen receptor status are prognostic and associated with poor prognosis in breast cancer liver metastases. Clin Exp Metastasis 33, 309–323.

Bocchi R, Egervari K, Carol-Perdiguer L, Viale B, Quairiaux C, De Roo M, Boitard M, Oskouie S, Salmon P, Kiss JZ (2017). Perturbed Wnt signaling leads to neuronal migration delay, altered interhemispheric connections and impaired social behavior. Nat Commun 8, 1158.

Boucaut JC, Darribere T (1983). Fibronectin in early amphibian embryos. Migrating mesodermal cells contact fibronectin established prior to gastrulation. Cell Tissue Res 234, 135–145.

Bronsert P, Enderle-Ammour K, Bader M, Timme S, Kuehs M, Csanadi A, Kayser G, Kohler I, Bausch D, Hoeppner J, *et al.* (2014). Cancer cell invasion and EMT marker expression: a three-dimensional study of the human cancer-host interface. J Pathol 234, 410–422.

Carvalho JR, Fortunato IC, Fonseca CG, Pezzarossa A, Barbacena P, Dominguez-Cejudo MA, Vasconcelos FF, Santos NC, Carvalho FA, Franco CA (2019). Non-canonical Wnt signaling regulates junctional mechanocoupling during angiogenic collective cell migration. eLife 8, e45853.

Cheung KJ, Gabrielson E, Werb Z, Ewald AJ (2013). Collective invasion in breast cancer requires a conserved basal epithelial program. Cell 155, 1639–1651.
Chiang AC, Massague J (2008). Molecular basis of metastasis. N Engl J Med 359, 2814–2823.
Colpaert CG, Vermeulen PB, Fox SB, Harris AL, Dirix LY, Van Marck EA (2003). The presence of a fibrotic focus in invasive breast carcinoma correlates with the expression of carbonic anhydrase IX and is a marker of hypoxia and poor prognosis. Breast Cancer Res Treat 81, 137–147.
Conklin MW, Eickhoff JC, Riching KM, Pehlke CA, Eliceiri KW, Provenzano PP, Friedl A, Keely PJ (2011). Aligned collagen is a prognostic signature for survival in human breast carcinoma. Am J Pathol 178, 1221–1232.
Cox TR, Erler JT (2011). Remodeling and homeostasis of the extracellular matrix: implications for fibrotic diseases and cancer. Dis Model Mech 4, 165–178.
Davidson LA, Dzamba BD, Keller R, Desimone DW (2008). Live imaging of cell protrusive activity, and extracellular matrix assembly and remodeling during morphogenesis in the frog, Xenopus laevis. Dev Dyn 237, 2684–2692.
Dohn MR, Mundell NA, Sawyer LM, Dunlap JA, Jessen JR (2013). Planar cell polarity proteins differentially regulate extracellular matrix organization and assembly during zebrafish gastrulation. Dev Biol 383, 39–51.
Dzamba BJ, Jakab KR, Marsden M, Schwartz MA, DeSimone DW (2009). Cadherin adhesion, tissue tension, noncanonical Wnt signaling regulate fibronectin matrix organization. Dev Cell 16, 421–432.
Erdogan B, Ao M, White LM, Means AL, Brewer BM, Yang L, Washington MK, Shi C, Franco OE, Weaver AM, *et al.* (2017). Cancer-associated fibroblasts promote directional cancer cell migration by aligning fibronectin. J Cell Biol 216, 3799–3816.
Erler JT, Bennewith KL, Cox TR, Lang G, Bird D, Koong A, Le QT, Giaccia AJ (2009). Hypoxia-induced lysyl oxidase is a critical mediator of bone marrow cell recruitment to form the premetastatic niche. Cancer Cell 15, 35–44.
Fane ME, Chhabra Y, Alicea GM, Maranto DA, Douglass SM, Webster MR, Rebecca VW, Marino GE, Almeida F, Ecker BL, *et al.* (2022). Stromal changes in the aged lung induce an emergence from melanoma dormancy. Nature 606, 396–405.
Franz CM, Jones GE, Ridley AJ (2002). Cell migration in development and disease. Dev Cell 2, 153–158.
Friedl P (2004). Prespecification and plasticity: shifting mechanisms of cell migration. Curr Opin Cell Biol 16, 14–23.
Friedl P, Alexander S (2011). Cancer invasion and the microenvironment: plasticity and reciprocity. Cell 147, 992–1009.
Friedl P, Gilmour D (2009). Collective cell migration in morphogenesis, regeneration and cancer. Nat Rev Mol Cell Biol 10, 445–457.
Ghajar CM, Peinado H, Mori H, Matei IR, Evason KJ, Brazier H, Almeida D, Koller A, Hajjar KA, Stainier DY, *et al.* (2013). The perivascular niche regulates breast tumour dormancy. Nat Cell Biol 15, 807–817.
Gopal S, Veracini L, Grall D, Butori C, Schaub S, Audebert S, Camoin L, Baudelet E, Radwanska A, Beghelli-de la Forest Divonne S, *et al.* (2017). Fibronectin-guided migration of carcinoma collectives. Nat Commun 8, 14105.
Grasset EM, Dunworth M, Sharma G, Loth M, Tandurella J, Cimino-Mathews A, Gentz M, Bracht S, Haynes M, Fertig EJ, Ewald AJ (2022). Triple-negative breast cancer metastasis involves complex epithelial-mesenchymal transition dynamics and requires vimentin. Sci Transl Med 14, eabn7571.
Grigore AD, Jolly MK, Jia D, Farach-Carson MC, Levine H (2016). Tumor budding: the name is EMT. Partial EMT. J Clin Med 5, 51.
Guo M, Ma G, Zhang X, Tang W, Shi J, Wang Q, Cheng Y, Zhang B, Xu J (2020). ROR2 knockdown suppresses breast cancer growth through PI3K/ATK signaling. Aging 12, 13115–13127.
Heremans A, De Cock B, Cassiman JJ, Van den Berghe H, David G (1990). The core protein of the matrix-associated heparan sulfate proteoglycan binds to fibronectin. J Biol Chem 265, 8716–8724.
Herschkowitz JI, Simin K, Weigman VJ, Mikaelian I, Usary J, Hu Z, Rasmussen KE, Jones LP, Assefnia S, Chandrasekharan S, *et al.* (2007). Identification of conserved gene expression features between murine mammary carcinoma models and human breast tumors. Genome Biol 8, R76.
Herschkowitz JI, Zhao W, Zhang M, Usary J, Murrow G, Edwards D, Knezevic J, Greene SB, Darr D, Troester MA, *et al.* (2012). Comparative oncogenomics identifies breast tumors enriched in functional tumor-initiating cells. Proc Natl Acad Sci USA 109, 2778–2783.
Hoschuetzky H, Aberle H, Kemler R (1994). Beta-catenin mediates the interaction of the cadherin-catenin complex with epidermal growth factor receptor. J Cell Biol 127, 1375–1380.
Huang DW, Sherman BT, Lempicki RA (2009). Systematic and integrative analysis of large gene lists using DAVID bioinformatics resources. Nat Protoc 4, 44–57.
Hynes RO (1992). Integrins: versatility, modulation, and signaling in cell adhesion. Cell 69, 11–25.
Jerry DJ, Kittrell FS, Kuperwasser C, Laucirica R, Dickinson ES, Bonilla PJ, Butel JS, Medina D (2000). A mammary-specific model demonstrates the role of the p53 tumor suppressor gene in tumor development. Oncogene 19, 1052–1058.
Joshi R, Goihberg E, Ren W, Pilichowska M, Mathew P (2017). Proteolytic fragments of fibronectin function as matrikines driving the chemotactic affinity of prostate cancer cells to human bone marrow mesenchymal stromal cells via the alpha5beta1 integrin. Cell Adh Migr 11, 305–315.
Kadler KE, Hill A, Canty-Laird EG (2008). Collagen fibrillogenesis: fibronectin, integrins, and minor collagens as organizers and nucleators. Curr Opin Cell Biol 20, 495–501.
Kai F, Drain AP, Weaver VM (2019). The extracellular matrix modulates the metastatic journey. Dev Cell 49, 332–346.
Kanellos G, Frame MC (2016). Cellular functions of the ADF/cofilin family at a glance. J Cell Sci 129, 3211–3218.
Kauppila S, Stenback F, Risteli J, Jukkola A, Risteli L (1998). Aberrant type I and type III collagen gene expression in human breast cancer in vivo. J Pathol 186, 262–268.
Kouros-Mehr H, Werb Z (2006). Candidate regulators of mammary branching morphogenesis identified by genome-wide transcript analysis. Dev Dyn 235, 3404–3412.
Kroger C, Afeyan A, Mraz J, Eaton EN, Reinhardt F, Khodor YL, Thiru P, Bierie B, Ye X, Burge CB, Weinberg RA (2019). Acquisition of a hybrid E/M state is essential for tumorigenicity of basal breast cancer cells. Proc Natl Acad Sci USA 116, 7353–7362.
Kumawat K, Menzen MH, Bos IS, Baarsma HA, Borger P, Roth M, Tamm M, Halayko AJ, Simoons M, Prins A, *et al.* (2013). Noncanonical WNT-5A signaling regulates TGF-beta-induced extracellular matrix production by airway smooth muscle cells. FASEB J 27, 1631–1643.
Lai SL, Chien AJ, Moon RT (2009). Wnt/Fz signaling and the cytoskeleton: potential roles in tumorigenesis. Cell Res 19, 532–545.
Langerod A, Zhao H, Borgan O, Nesland JM, Bukholm IR, Ikdahl T, Karesen R, Borresen-Dale AL, Jeffrey SS (2007). TP53 mutation status and gene expression profiles are powerful prognostic markers of breast cancer. Breast Cancer Res 9, R30.
le Duc Q, Shi Q, Blonk I, Sonnenberg A, Wang N, Leckband D, de Rooij J (2010). Vinculin potentiates E-cadherin mechanosensing and is recruited to actin-anchored sites within adherens junctions in a myosin II-dependent manner. J Cell Biol 189, 1107–1115.
Levental KR, Yu H, Kass L, Lakins JN, Egeblad M, Erler JT, Fong SF, Csiszar K, Giaccia A, Weninger W, *et al.* (2009). Matrix crosslinking forces tumor progression by enhancing integrin signaling. Cell 139, 891–906.
Luond F, Sugiyama N, Bill R, Bornes L, Hager C, Tang F, Santacroce N, Beisel C, Ivanek R, Burglin T, *et al.* (2021). Distinct contributions of partial and full EMT to breast cancer malignancy. Dev Cell 56, 3203–3221.e11.
Mani SA, Guo W, Liao MJ, Eaton EN, Ayyanan A, Zhou AY, Brooks M, Reinhard F, Zhang CC, Shipitsin M, *et al.* (2008). The epithelial-mesenchymal transition generates cells with properties of stem cells. Cell 133, 704–715.
Manie E, Vincent-Salomon A, Lehmann-Che J, Pierron G, Turpin E, Warcoin M, Gruel N, Lebigot I, Sastre-Garau X, Lidereau R, *et al.* (2009). High frequency of TP53 mutation in BRCA1 and sporadic basal-like carcinomas but not in BRCA1 luminal breast tumors. Cancer Res 69, 663–671.
Marusyk A, Janiszewska M, Polyak K (2020). Intratumor heterogeneity: the Rosetta stone of therapy resistance. Cancer Cell 37, 471–484.
McLean GW, Carragher NO, Avizienyte E, Evans J, Brunton VG, Frame MC (2005). The role of focal-adhesion kinase in cancer—a new therapeutic opportunity. Nat Rev Cancer 5, 505–515.
Menck K, Heinrichs S, Wlochowitz D, Sitte M, Noeding H, Janshoff A, Treiber H, Ruhwedel T, Schatlo B, von der Brelie C, *et al.* (2021). WNT11/ROR2 signaling is associated with tumor invasion and poor survival in breast cancer. J Exp Clin Cancer Res 40, 395.
Miettinen PJ, Ebner R, Lopez AR, Derynck R (1994). TGF-beta induced transdifferentiation of mammary epithelial cells to mesenchymal cells: involvement of type I receptors. J Cell Biol 127, 2021–2036.
Missirlis D, Haraszti T, Kessler H, Spatz JP (2017). Fibronectin promotes directional persistence in fibroblast migration through interactions with both its cell-binding and heparin-binding domains. Sci Rep 7, 3711.
Nieto MA, Huang RY, Jackson RA, Thiery JP (2016). EMT: 2016. Cell 166, 21–45.

Onder TT, Gupta PB, Mani SA, Yang J, Lander ES, Weinberg RA (2008). Loss of E-cadherin promotes metastasis via multiple downstream transcriptional pathways. Cancer Res 68, 3645–3654.
Osmani N, Follain G, Garcia Leon MJ, Lefebvre O, Busnelli I, Larnicol A, Harlepp S, Goetz JG (2019). Metastatic tumor cells exploit their adhesion repertoire to counteract shear forces during intravascular arrest. Cell Rep 28, 2491–2500.e2495.
Padmanaban V, Krol I, Suhail Y, Szczerba BM, Aceto N, Bader JS, Ewald AJ (2019). E-cadherin is required for metastasis in multiple models of breast cancer. Nature 573, 439–444.
Pankov R, Cukierman E, Katz BZ, Matsumoto K, Lin DC, Lin S, Hahn C, Yamada KM (2000). Integrin dynamics and matrix assembly: tensin-dependent translocation of alpha(5)beta(1) integrins promotes early fibronectin fibrillogenesis. J Cell Biol 148, 1075–1090.
Parisi L, Toffoli A, Ghezzi B, Mozzoni B, Lumetti S, Macaluso GM (2020). A glance on the role of fibronectin in controlling cell response at biomaterial interface. Jpn Dent Sci Rev 56, 50–55.
Pastushenko I, Mauri F, Song Y, de Cock F, Meeusen B, Swedlund B, Impens F, Van Haver D, Opitz M, Thery M, *et al.* (2021). Fat1 deletion promotes hybrid EMT state, tumour stemness and metastasis. Nature 589, 448–455.
Perou CM, Sorlie T, Eisen MB, van de Rijn M, Jeffrey SS, Rees CA, Pollack JR, Ross DT, Johnsen H, Akslen LA, *et al.* (2000). Molecular portraits of human breast tumours. Nature 406, 747–752.
Pickup MW, Mouw JK, Weaver VM (2014). The extracellular matrix modulates the hallmarks of cancer. EMBO Rep 15, 1243–1253.
Provenzano PP, Inman DR, Eliceiri KW, Knittel JG, Yan L, Rueden CT, White JG, Keely PJ (2008). Collagen density promotes mammary tumor initiation and progression. BMC Med 6, 11.
Qian X, Karpova T, Sheppard AM, McNally J, Lowy DR (2004). E-cadherin-mediated adhesion inhibits ligand-dependent activation of diverse receptor tyrosine kinases. EMBO J 23, 1739–1748.
Roarty K, Pfefferle AD, Creighton CJ, Perou CM, Rosen JM (2017). Ror2-mediated alternative Wnt signaling regulates cell fate and adhesion during mammary tumor progression. Oncogene 36, 5958–5968.
Roarty K, Shore AN, Creighton CJ, Rosen JM (2015). Ror2 regulates branching, differentiation, and actin-cytoskeletal dynamics within the mammary epithelium. J Cell Biol 208, 351–366.
Rottenberg S, Jaspers JE, Kersbergen A, van der Burg E, Nygren AO, Zander SA, Derksen PW, de Bruin M, Zevenhoven J, Lau A, *et al.* (2008). High sensitivity of BRCA1-deficient mammary tumors to the PARP inhibitor AZD2281 alone and in combination with platinum drugs. Proc Natl Acad Sci USA 105, 17079–17084.
Schlessinger K, Hall A, Tolwinski N (2009). Wnt signaling pathways meet Rho GTPases. Genes Dev 23, 265–277.
Sechler JL, Takada Y, Schwarzbauer JE (1996). Altered rate of fibronectin matrix assembly by deletion of the first type III repeats. J Cell Biol 134, 573–583.
Sidani M, Wessels D, Mouneimne G, Ghosh M, Goswami S, Sarmiento C, Wang W, Kuhl S, El-Sibai M, Backer JM, *et al.* (2007). Cofilin determines the migration behavior and turning frequency of metastatic cancer cells. J Cell Biol 179, 777–791.
Sottile J, Hocking DC (2002). Fibronectin polymerization regulates the composition and stability of extracellular matrix fibrils and cell-matrix adhesions. Mol Biol Cell 13, 3546–3559.
Spill F, Reynolds DS, Kamm RD, Zaman MH (2016). Impact of the physical microenvironment on tumor progression and metastasis. Curr Opin Biotechnol 40, 41–48.
Suarez-Arnedo A, Figueroa FT, Clavijo C, Arbelaez P, Cruz JC, Munoz-Camargo C (2020). An Image J plugin for the high throughput image analysis of in vitro scratch wound healing assays. PLoS One 15, e0232565.
Takeichi M (1991). Cadherin cell adhesion receptors as a morphogenetic regulator. Science 251, 1451–1455.
The Cancer Genome Atlas Network (2012). Comprehensive molecular portraits of human breast tumours. Nature 490, 61–70.
Ulrich F, Krieg M, Schotz EM, Link V, Castanon I, Schnabel V, Taubenberger A, Mueller D, Puech PH, Heisenberg CP (2005). Wnt11 functions in gastrulation by controlling cell cohesion through Rab5c and E-cadherin. Dev Cell 9, 555–564.
van Amerongen R, Fuerer C, Mizutani M, Nusse R (2012). Wnt5a can both activate and repress Wnt/beta-catenin signaling during mouse embryonic development. Dev Biol 369, 101–114.
van Amerongen R, Nusse R (2009). Towards an integrated view of Wnt signaling in development. Development 136, 3205–3214.
Van Obberghen-Schilling E, Tucker RP, Saupe F, Gasser I, Cseh B, Orend G (2011). Fibronectin and tenascin-C: accomplices in vascular morphogenesis during development and tumor growth. Int J Dev Biol 55, 511–525.
Vega ME, Schwarzbauer JE (2016). Collaboration of fibronectin matrix with other extracellular signals in morphogenesis and differentiation. Curr Opin Cell Biol 42, 1–6.
Wehner D, Tsarouchas TM, Michael A, Haase C, Weidinger G, Reimer MM, Becker T, Becker CG (2017). Wnt signaling controls pro-regenerative collagen XII in functional spinal cord regeneration in zebrafish. Nat Commun 8, 126.
Williams ED, Gao D, Redfern A, Thompson EW (2019). Controversies around epithelial-mesenchymal plasticity in cancer metastasis. Nat Rev Cancer 19, 716–732.
Wu C, Bauer JS, Juliano RL, McDonald JA (1993). The alpha 5 beta 1 integrin fibronectin receptor, but not the alpha 5 cytoplasmic domain, functions in an early and essential step in fibronectin matrix assembly. J Biol Chem 268, 21883–21888.
Zhang M, Behbod F, Atkinson RL, Landis MD, Kittrell F, Edwards D, Medina D, Tsimelzon A, Hilsenbeck S, Green JE, *et al.* (2008). Identification of tumor-initiating cells in a p53-null mouse model of breast cancer. Cancer Res 68, 4674–4682.